Sputtered II-VI Alloys and Structures for Tandem PV

Final Subcontract Report
9 December 2003 – 30 July 2007

A.D. Compaan, R. Collins, V.G. Karpov, and
D. Giolando
University of Toledo
Toledo, Ohio

Sputtered II-VI Alloys and Structures for Tandem PV

Final Subcontract Report
9 December 2003 – 30 July 2007

A.D. Compaan, R. Collins, V.G. Karpov, and
D. Giolando
*University of Toledo*
Toledo, Ohio

NREL Technical Monitor: Fannie Eddy

Prepared under Subcontract No. XAT-4-33624-06

National Renewable Energy Laboratory
1617 Cole Boulevard, Golden, Colorado 80401-3393
303-275-3000 • www.nrel.gov

Operated for the U.S. Department of Energy
Office of Energy Efficiency and Renewable Energy
by Midwest Research Institute • Battelle

Contract No. DE-AC36-99-GO10337
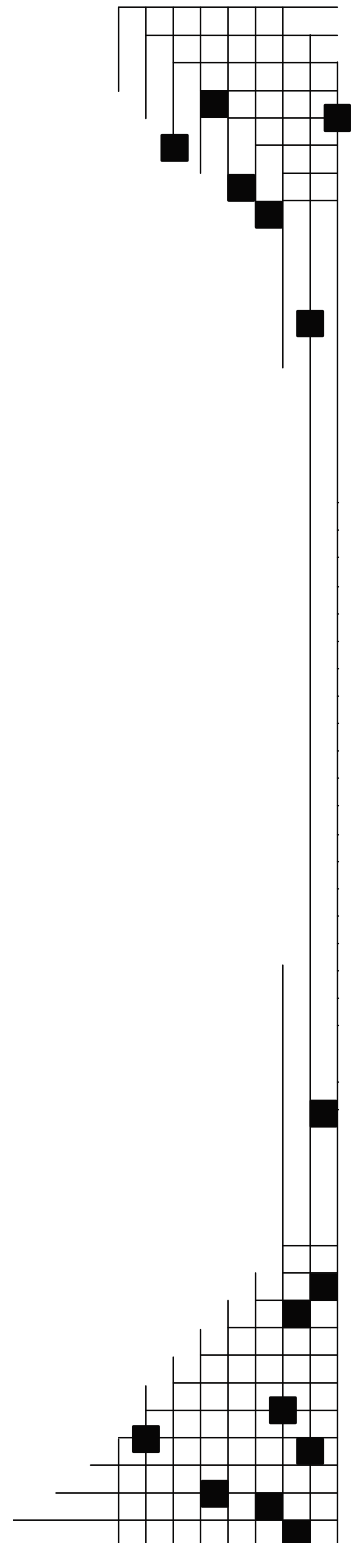
**This publication was reproduced from the best available copy
submitted by the subcontractor and received no editorial review at NREL**

NOTICE

This report was prepared as an account of work sponsored by an agency of the United States government. Neither the United States government nor any agency thereof, nor any of their employees, makes any warranty, express or implied, or assumes any legal liability or responsibility for the accuracy, completeness, or usefulness of any information, apparatus, product, or process disclosed, or represents that its use would not infringe privately owned rights. Reference herein to any specific commercial product, process, or service by trade name, trademark, manufacturer, or otherwise does not necessarily constitute or imply its endorsement, recommendation, or favoring by the United States government or any agency thereof. The views and opinions of authors expressed herein do not necessarily state or reflect those of the United States government or any agency thereof.

Available electronically at http://www.osti.gov/bridge

Available for a processing fee to U.S. Department of Energy
and its contractors, in paper, from:
       U.S. Department of Energy
       Office of Scientific and Technical Information
       P.O. Box 62
       Oak Ridge, TN 37831-0062
       phone: 865.576.8401
       fax: 865.576.5728
       email: mailto:reports@adonis.osti.gov

Available for sale to the public, in paper, from:
       U.S. Department of Commerce
       National Technical Information Service
       5285 Port Royal Road
       Springfield, VA 22161
       phone: 800.553.6847
       fax: 703.605.6900
       email: orders@ntis.fedworld.gov
       online ordering: http://www.ntis.gov/ordering.htm

Printed on paper containing at least 50% wastepaper, including 20% postconsumer waste

Goals and Objectives

The major objectives of this subcontract are to explore, prepare and test the candidate materials of II-VI group for top cells in two-junction devices with either monolithic two-terminal or mechanically stacked four-terminal structures. We have developed two candidate alloys CdMnTe and CdMgTe by RF sputtering. The critical chloride treatments and related material studies revealed that CdMgTe is superior to CdMnTe. In the second year of this project much of the efforts were to develop the CdMgTe alloy. The goal of these efforts is to optimize the film deposition conditions, chloride treatments and identify the efficiency limiting factors in a single junction CdTe/CdS device, which can lead to the goal of 25% efficient tandem structures fabricated using polycrystalline thin films.

This subcontract consists of three one-year phases incrementally funded. The present report is the final report covering all three Phases. This report will elaborate on Phase Three and provide appropriate summaries of the first two Phases. During Phase Three of the subcontract, the research work was divided into five task areas covering different aspects of a tandem cell. The fist task area covered sputtered II-VI materials and cells and incorporated Tasks 1 (Yr1), 6 (Yr 2), and 11 (Yr 3). The second task area covered transparent contact/window layers and recombination junctions and incorporated Tasks 2, 7, and 12 (Yr 3). The third task area covered interconnect studies and related nonideal tandem cell modeling and included Tasks 3, 8, and 13 (Yr 3). Task area four covered mercury cadmium telluride and bottom cells and included Tasks 4, 9, and 14 (Yr 3). Finally task area five covered characterization and stress studies and included Tasks 5, 10, and 15 (Yr 3).

Executive Summary/Major Accomplishments

The following are the major accomplishments during the 44 months of this subcontract:

Tasks 1, 6, 11 Sputtered top cell II-VI alloy materials and cells

Task 1: *Sputtered top cell II-VI alloys (Phase I)*
- Post deposition treatment conditions for cells with thinner CdTe layer (< 1 μm thick) were optimized. An efficiency of 11.8% was achieved using only a 0.87 μm CdTe layer in place of our standard 2.3 μm.
- Real time spectroscopic ellipsometry (RTSE) has been installed for the first time onto a two-chamber magnetron sputtering system for the fabrication of polycrystalline II-VI solar cells incorporating CdTe and related ternary alloys. In addition to in-depth optical analyses of the solar-cell materials and their interfaces, RTSE can also be used for routine tasks such as substrate temperature and deposition rate calibrations.
- In initial RTSE studies of the growth of CdTe on test c-Si wafers and on superstrate Mo substrates, the evolution of film microstructure has been characterized. As-deposited CdTe films exhibit density deficits as high as 10% relative to the single crystal. Such density deficits depend sensitively on the thickness during growth and on the nature of the substrate. In future work, the effect of void fraction profiles in CdS and CdTe on post-deposition processing and on ultimate device performance will be evaluated.
- In initial RTSE studies of CdTe and CdS on test c-Si wafers, the real and imaginary parts of the dielectric functions of the films have been extracted from measurements performed in real time. Although the fundamental absorption onset in CdTe is sharp and not very sensitive to thickness and fabrication procedure, the widths and amplitudes of the high energy critical point transitions (E_1, $E_1+\Delta_1$ and E_2) vary considerably, and thus are expected to provide information on defect density, grain size, and grain orientation in future studies.
- High quality films of CdMnTe were obtained from a sintered target composed of 13% MnTe and 87% CdTe. Two different types of post-deposition chloride treatments were done, and results were analyzed using a variety of characterization techniques. The composition of Mn in the films is reduced during chloride treatment, and hence the bandgap of the films shifted towards CdTe. Although some improvement in cell performance was observed due to Cu doping, the V_{OC}, J_{SC} and FF were still very low in comparison to pure CdTe cells.

Task 6: *Sputtered top cell II-VI alloys (Phase II)*
1. **Baseline conditions for the sputter deposition of the alloy $Cd_{1-x}Mg_xTe$ have been established.**
- Deposition temperature higher than 250 $^{\circ}$C is needed to obtain polycrystalline films. Films deposited below 250 $^{\circ}$C are mixtures of amorphous and polycrystalline phases.
- Film deposition rate is lower for CdMgTe than for CdTe. The deposition rate was about 0.45 μm/hour for RF power of 50W with deposition temperatures in the range between 275 to 300 $^{\circ}$C. Ar was the sputter gas, and the deposition pressure was between 5 and 20 mTorr.

2. **Polycrystalline thin films of $Cd_{0.95}Mg_{0.05}Te$ were sputter deposited and the structural, optical and morphological properties were studied.**

- XRD studies showed polycrystalline films with strong preference for (111) plane.
- Films deposited above 250 ^{o}C have sharp band edge absorption consistent with a direct band gap.
- The band gap of the film was estimated as 1.58 eV from the transmittance spectra.
- The Mg content of the film was estimated as a function of band gap, the obtained value of 5% is comparable with the average value (8 ±2 %) obtained from energy dispersive x-ray spectroscopy (EDS) measurements.
- AFM studies revealed a compact and smooth surface. The average peak-to-valley depth of a 2 μm thick film was about 60 nm.
- Raman spectra exhibit a sharp (FWHM=9 cm^{-1}) and symmetric band corresponding to the CdTe-like LO modes indicating a good polycrystalline nature of the film.
- The influence of the sputter gas (Ar and Ne) on the deposition and film growth was analyzed. Ne sputtered films show a slight increase in band gap (0.01eV), which can be due to an increase in the sputter yield of Mg relative to Cd when Ne is used. This is possible since the atomic mass of Ne is close to that of Mg. However the film deposition rate is almost 25% lower with Ne than with Ar gas.
- AFM studies showed identical surface features for both Ar and Ne sputtered films.
- Hot probe tests showed that the as-deposited films are always p-type.

3. **Post deposition cadmium chloride vapor treatment of the alloy $Cd_{0.95}Mg_{0.05}Te$ was studied and the baseline conditions for film stability were established.**

- Conditions for the cadmium chloride annealing treatments were identified as: temperature- 387 ^{o}C, annealing duration- 5 to 10 minutes, separation between film and cadmium chloride source- 1 mm, dry air flow rate- 60 sccm.
- Longer annealing durations affect the stability of the films. Annealing durations greater than 10 minutes resulted in a decrease in band gap, approaching the value of CdTe. The mechanical stability of the film is unaffected by annealing duration and the material loss is negligible.
- AFM and XRD analyses show evidence of grain growth and recrystallization. The film crystallographic orientation became more random with annealing duration.

4. Prototype top cells

- A prototype top sub-cell of the configuration TEC-7/CdS/$Cd_{0.95}Mg_{0.05}Te$/Cu/Au has shown promising photovoltaic activity. We obtained the following device parameters under 1 sun illumination: V_{oc}=630 mV, J_{sc}=17 mA/cm^2, FF=36%, efficiency= 3.8%. The quantum efficiency of the device has better blue response compared to CdTe/CdS devices.
- We have developed a CdTe/CdS cell with thin CdTe (0.87 μm) for possible application as a top sub-cell. This device showed 11.8% efficiency with V_{oc}=772 mV, J_{sc}=22 mA/cm^2, and FF=69.7%.

Task 11: *Sputtered top cell II-VI alloys, including graded structures (PhaseIII)*

- We have used optical emission spectroscopy of the plasma to relate the emission intensities from Mg I, Cd II, Te II, and Ar I as a function of argon pressure and RF power to the characteristics of the films including strain, Mg composition and band gap.
- X-ray diffraction and atomic force microscopy studies of as-grown films show decreasing grain size as RF power increases and as Ar pressure decreases. Simultaneously the crystallographic morphology transitions from cubic to hexagonal.
- Two to five minutes of $CdCl_2$ activation near 387 ^{o}C improves the device performance but our device efficiency has not exceeded 4% at AM1.5, but the subgap transmission ($\lambda \geq 750$ nm) is about 75% for 0.66 µm thick CdMgTe.
- We find the most promising approach to a polycrystalline thin-film tandem is to use extremely thin (~0.3µm) CdTe together with a CIS bottom cell in a four-terminal configuration or together with a HgCdTe bottom cell in a two-terminal configuration.

Tasks 2, 7, 12 Transparent contacts/window layers & recombination junctions

Task 2: *Transparent contacts/window layers and recombination junctions (Phase I)*

- Reactive sputtering deposition conditions were optimized to obtain a ZnO HRT layer from a conducting ZnO:Al target. The cells prepared using this ZnO HRT and thinner CdS layer showed increased V_{OC}, J_{SC} and efficiency in comparison to cells without the HRT layer but with the same CdS thickness.
- ZnTe:Cu films were sputter-deposited and characterized for electrical and optical properties to be used as the p-type layer of a recombination junction. Post-deposition diffusion conditions were optimized after deposition on a sputtered CdS/CdTe top cell.
- Monolithic two-terminal tandem cells were fabricated using a CdS/CdTe top cell and a CdS/HgCdTe bottom cell. Two types of recombination junctions, ZnTe:N/ZnO:Al and ZnTe:Cu/ZnO:Al, were used and tandem cell performances were compared. The ZnTe:N based recombination junction showed better results, possibly due to some Cu out-diffusion from the ZnTe:Cu-based recombination junction into the top cell or bottom cell junction during fabrication of the bottom CdS/HgCdTe cell.

Task 7: *Transparent contacts/window layers and recombination junctions (Phase II)*

- Comparison studies were made of ZnO:Al, ZnTe:N/ZnO:Al, ITO, and ZnTe:N/ITO as back contact structures to superstrate CdTe top cells. We found the best performance with the ZnTe:N/ITO bilayer.
- The best efficiency with this ZnTe:N/ITO transparent back contact was 9.1% with most of the difference from our typical 12% efficiency using Cu/Au contacts due to poor voltage ($V_{OC} = 643$ mV). No copper was used in this contact.

Task 12: *Transparent contacts/window layers and recombination junctions (Phase III)*

- We adjusted the resistivity of RF sputtered ITO over more than two decades by controlling the deposition temperature and found that the best transparent back contact performance was achieved at intermediate conductivity ($\sigma \approx 10^2$ S/cm) with a 0.5 µm thick film having a sheet resistance of 200 $\Omega/\square$.

Tasks 3, 8, 13 Interconnect studies and related nonideal tandem cell modeling

Task 3: *Interconnect studies and related nonideal tandem cell modeling (Phase I)*
- A new physical mechanism of current flow in polycrystalline interconnects is proposed and analytically described, based on hopping electron transport through defect chains of abnormally low resistance (pinholes). The integral electrical parameters of such interconnects are estimated for the materials used in our tandem cells.
- Interconnect-related power loss is estimated to be surprisingly low (on the order of 1 relative percent) for polycrystalline interconnects of considerable thickness (100 nm). This new understanding predicts reproducible and robust polycrystalline interconnects.

Task 8: *Interconnect studies and related nonideal tandem cell modeling (Phase II)*
- A prototype tunneling junction structure of rf-sputtered CdTe sandwiched between two Cr metal electrodes was studied in the AFM current-sensing mode measuring the local current-voltage characteristics and electric current variations with time under fixed voltage.
- The observed lateral nonuniformity in the AFM current-voltage characteristics and chaotic temporal variations of the AFM current did not correlate with the surface topography and can be interpreted in the terms of defect assisted tunneling through time-dependent defect pathways.
- The latter transport mechanism underlies the possibility of efficient low-resistance interconnects in submicron thickness range readily made by the existing polycrystalline film deposition techniques. This range of thickness goes far beyond that of standard tunnel junctions (thinner than 0.01 micron) and opens new venues in the tandem junction interconnect technology.

Task 13: *Interconnect studies and related nonideal tandem cell modeling (Phase III)*
- Optical Modeling of II-VI Tandem Device Performance

Tasks 4, 9, 14 HgCdTe bottom cell studies/back contact

Task 4: *HgCdTe bottom cell studies/back contact (Phase I)*

This task was not active during Phase I.

Task 9: *HgCdTe bottom cell studies/back contact (Phase II)*
- A commercially prepared target was obtained with composition $Hg_{40}Cd_{60}Te$ and several devices were prepared. $CdCl_2$ treatments appear to work well and several cells were prepared with back contacts of Mo, Au, and Cr, both with 2-3 nm of Cu and without a Cu interlayer.
- Devices prepared with Cu/Au back contacts were best and showed QE response to 1150 nm. However, the devices had poor current collection and fill factors.

Task 14: *HgCdTe bottom cell studies/back contact (Phase III)*
- With careful choice of deposition temperature and target alloy composition the film quality was improved. We have fabricated CdS/CdTe/HgCdTe cells with efficiencies up to 6.7% and spectral response out to ~1100 nm. Best results were obtained with a thin (~0.2 μm) CdTe buffer layer at the junction with CdS. This suggests that an alloy compositional gradient could be effective in achieving higher efficiencies.
- Light soak studies of unencapsulated CdS/HgCdTe cells in summer air (typically 60% RH) indicate good stability for 1000 hours of continuous light soak at one-sun illumination.

Tasks 5, 10, 15 Characterization and stress studies

Task 5: *Characterization and Stress Studies (Phase I)*
- Ex situ spectroscopic ellipsometry (SE) has been applied in initial studies to determine the optical properties of the component materials of CdTe based solar cells. These results are necessary for a full accounting of optical losses and gains in single junction and tandem solar cells; thus, they are also necessary in the optimization of advanced optical designs to improve the efficiency of the cells. In the initial studies, the optical properties of soda lime glass and the component layers of TEC-15 glass have been parameterized.

Task 10: *Characterization and Stress Studies (Phase II)*
- Work continued on building up a database of optical properties of the CdS, CdTe and alloy materials.
- A multilayer model with all the optical properties and surface roughness has been used to fit reflectance data and quantum efficiency data.

Task 15: *Characterization and Stress Studies (Phase III)*
- Real Time Spectroscopic Ellipsometry Studies of II-VI Alloy Films
- X-ray photoelectron spectroscopy of CdMgTe (Clemens Heske group at UNLV)
- Thin CdTe as a top cell (filter) over a Si wafer (Rohatgi/Yelundur, Georgia Tech)

Table of Contents

List of Figures

Section 5

Section 6

Section 7

List of Tables

1 Introduction

1.1 Background

The purpose of this subcontract is to: 1) develop low-temperature deposition methods for polycrystalline thin-film materials and structures that have the potential to produce tandem cells reaching 25% efficiency at AM1.5 while using processes that are compatible with a bottom cell of the chalcopyrite (e.g., CIS or CIGS) structure, 2) develop *in situ* spectroscopic ellipsometry for growth diagnostics and deposition control, as well as *ex situ* characterization using a variety of techniques, and 3) model nonuniformities in tandem structures.

This annual report covers the second phase (14 months) of a three-year, NREL High Performance PV Phase IB, "High Performance PV—Exploring and Accelerating Ultimate Pathways," subcontract XAT-4-33624-06 with The University of Toledo.

1.2 Objectives of this subcontract

A primary objective is to optimize low-temperature magnetron sputter deposition and post-deposition processing conditions for CdTe-related II-VI polycrystalline thin films. The materials emphases are being placed on CdMnTe and CdMgTe for top cells including exploration of their suitability for the substrate configuration needed for two-terminal devices when CIS is grown first. Low-temperature magnetron sputter deposition is likely to be a prime consideration for top cells fabricated on bottom cells such as CIS, which are known to deteriorate at elevated temperatures. A ZnO-based high resistivity transparent (HRT) layer was studied for use with a thin CdS layer and the CdTe-based layers. Other effort focused on fabricating and modeling tunnel/recombination junctions suitable for the II-VI alloy top cell – with a chalcopyrite bottom cell. During Phase Two effort was begun on exploring the potential for HgCdTe as a bottom cell with CdTe or suitable alloy as the top cell in a superstrate structure. *In situ* spectroscopic ellipsometry is being pursued as a tool for *in situ* deposition control and *ex situ* film characterization.

1.3 Technical approach

The major part of the work under this subcontract is divided into five tasks: (1) development of II-VI alloy materials (CdMgTe) and the optimization of thin CdTe layers for current matching with the bottom cell, (2) development of improved window/HRT/front contact layers and transparent back-contact/recombination junctions, (3) theoretical and modeling studies of tandem cell interconnects and modeling of tandem device with non-ideal, spatially nonuniform interconnects, (4) development of a superstrate-type bottom cell based on HgCdTe suitably matched to a II-VI top cell and identification of materials for low-resistance back contacts, and (5) characterization and stress studies, which include *ex situ* spectroscopic ellipsometry (SE) studies on the temperature dependence of the optical properties, development of a database for optical modeling of polycrystalline thin-film tandem cells.

2   *Sputtered II-VI alloys for top cells (Task 11)*
2.1.   **Sputter deposition of CdMgTe films**

During Phase II, we studied the properties and chloride treatment characteristics of CdMgTe films and devices prepared from a sputter target with 20% MgTe by weight. In Phase III, additional effort was placed on films sputtered from a 40% MgTe target by weight (60% CdTe by weight). Results have been presented in the Q1 and Q2 reports. Some highlights are reviewed here.

We found that the sputtering rate from both of these alloy targets to be much slower than from pure CdTe target. The film composition sputtered from the 20% MgTe target was typically 5% Mg, i.e., $Cd_{0.95}Mg_{0.05}Te$. From the 40% target, the as-deposited composition was typically 19±2%. The sputtered films were smooth and had well-behaved x-ray diffraction and optical absorption (see Figure 2.1.) but treatment in chloride vapors was very difficult (see Figure 2.2.)

Figure 2.1. The transmittance spectrum of a $Cd_{0.8}Mg_{0.2}Te$ film deposited on glass substrate at 275 °C, the inset is the $(\alpha h\upsilon)^2$ vs. $h\upsilon$ plot showing the band gap of the alloy material as 1.85 eV.
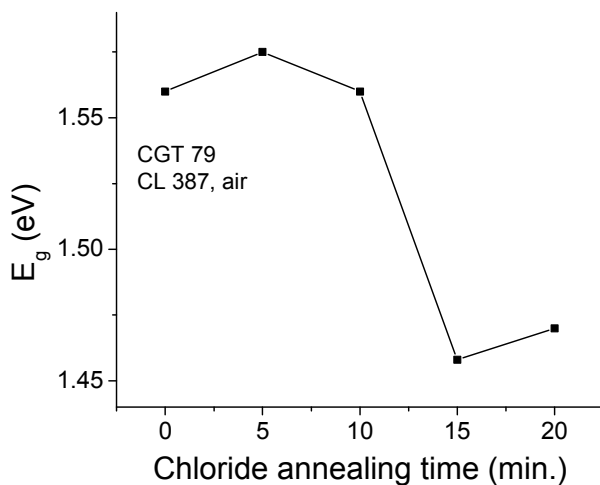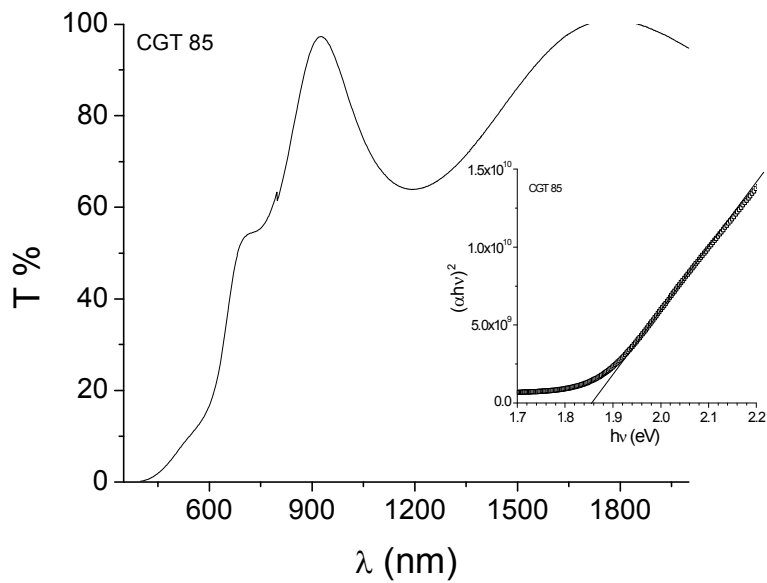
Figure 2.2. $Cd_{0.95}Mg_{0.05}Te$ film band-gap vs chloride annealing time at 387 °C in dry air. The film thickness was 0.4 μm.

As seen in Figure 2.2, the films would not tolerate more than about 10 minutes in chloride vapors when oxygen was also present. This is typical for post-deposition treatment for CdTe films. The x = 20% films ($E_g \approx 1.85$ eV) were even more sensitive to oxygen and were limited to about 3 minutes at 387 ^{o}C in dry air (see Figure 2.3.). Undoubtedly this is due to oxidation of the Mg; however, chloride treatments with the presence of some oxygen did not yield improvements to the photovoltaic performance. Therefore we found that adjusting the time and temperature to be within a narrow window and working with the lower magnesium content films to be the most productive.
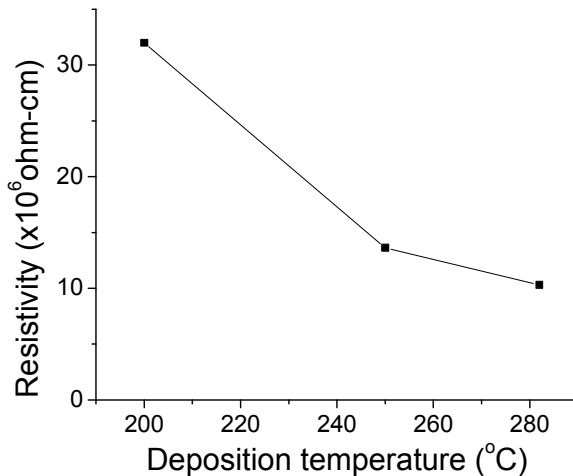
Figure 2.3. Dependence of sheet resistance on the film deposition temperature for films deposited from the 20 wt.% MgTe target.

In our Q2 report we indicated that the best results were obtained if the Mg alloy films were vacuum annealed at 400 ^{o}C for 30-40 minutes immediately after the deposition at 250 ^{o}C followed by a subsequent treatment in CdCl$_2$ vapor in dry air. This process applied to the 20% Mg films yielded cells with a performance of: V_{OC}=630 mV, J_{SC}=6.2 mA/cm^2, FF=38, η=1.5%. The 5% Mg films yielded the best cells and were reported in the Phase II Annual Report with η=3.3%.

At this point, although we have been able to deposit alloy films with up to 20% Mg, and having good crystallographic and optical properties, we have not been able to achieve suitable electronic properties (carrier lifetime, etc) to yield good solar cell performance, although the films are p-type as measured by the hot probe technique.

2.1.1 Optical emission spectroscopy as on-line probe of CdMgTe sputtering

Although success was limited in fabricating good devices from CdS/CdMgTe structures, we were able to demonstrate the utility of optical emission as a diagnostic of the sputtering plasma. This was discussed in Q4 report of Phase III and some illustrations are presented here.

Digital images of the RF plasma, Figure 2.4, show that the region of light emission expands with increasing power. As power increases with pressure held at 15 mTorr , green emission begins to dominate. The spectral identification, Figure 2.5, shows that the green emission is due to a strong Mg I emission that increases strongly with R.F. power. The intensity of each of the selected peaks increases with increase in r.f power with Ar pressure constant (15 mTorr). The intensity increase of the Ar signal reflects the increase in electron ionization and excitation from the high energy tail of the electron distribution. On the other hand, the Mg I, Cd II, and Te II species are sputtered from the target and increase in density with power. In addition the increased power also increases the fraction of excited and ionized atoms in the vapor.
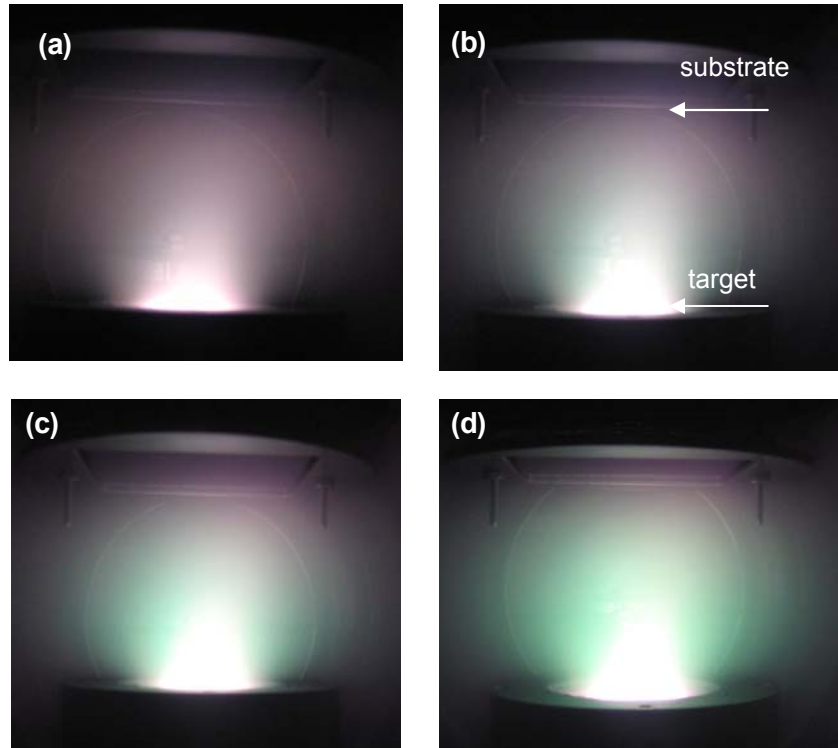
Figure 2.4 Images of plasma at 15 mTorr with RF power of: a) 15 W, b) 30 W, c) 50 W, and d) 70 W.

Figure 2.5. A sketch of the four transitions studied here with upper and lower energy states drawn to scale.
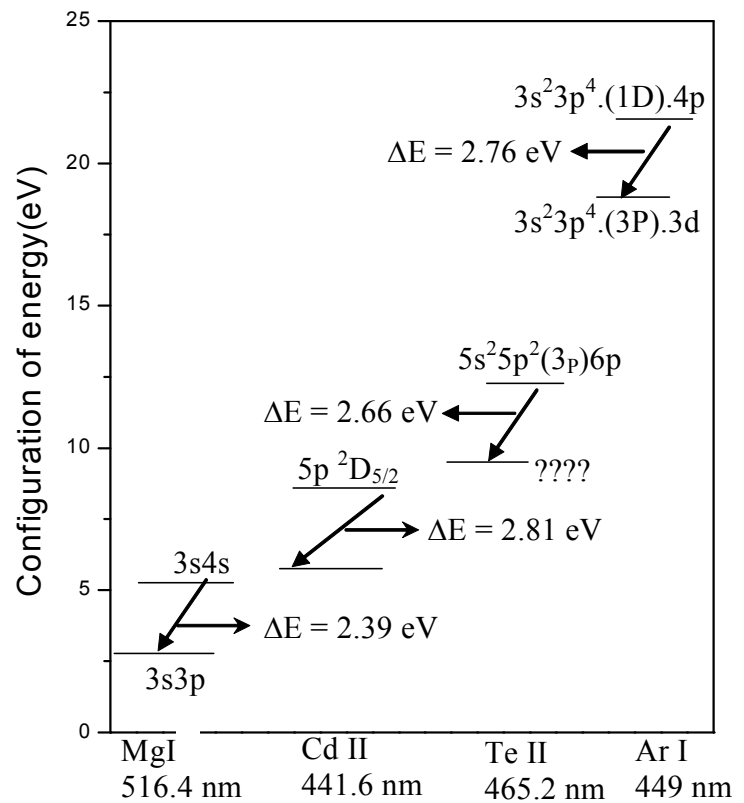
2.1.2 Growth rate

The growth rate as a function of R.F. power and as a function of sputter gas pressure are shown in Figure 6. The deposition rate increases monotonically with power but is sublinear above about 45 W of power into the 50 mm target. Above 30 mTorr excessive scattering in the Ar sputter gas decreases the growth rate.
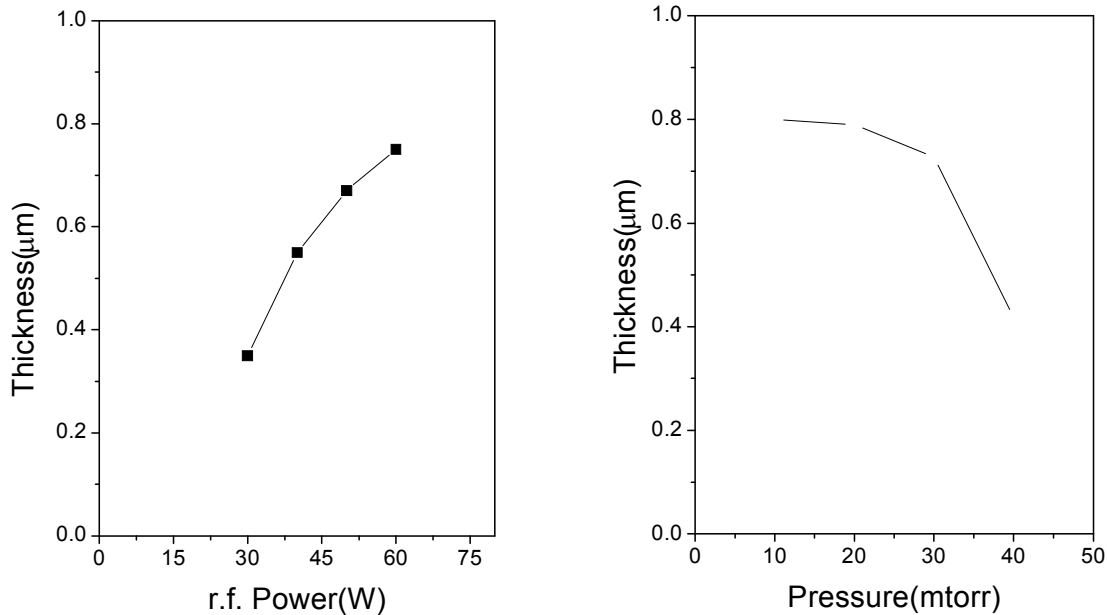
Figure 2.6. Thickness dependence of CdMgTe films a) with R.F. power at 15 mTorr and b) with Ar pressure at 50 W of RF power.

2.1.3 Lattice structure, optical absorption, and composition vs. sputter parameters

X-ray diffraction studies (see Figure 2.7.) of the CdMgTe films deposited at 300 ^{o}C from the 40 wt% MgTe sintered target (MgTe + CdTe) indicate a mixture of cubic and hexagonal phases. Phase identification is based on corresponding structures in the binary CdTe. The peaks ~ 22.54^o indicate 100(hexagonal) plane of CdTe and ~23.79^o indicates 111(cubic) plane of CdTe. With film thicknesses of about one micron, other prominent peaks arise from the commercial tin oxide substrate: at ~26.54^o from Sn_2O_3 (011), ~37.7^o from SnO_2 (200), ~51.45^o from SnO_2 (211), ~54.45^o from SnO_2 (220) and ~65.5^o from SnO_2 (222). The data indicate an increasing fraction of hexagonal phase as the power increases from 30W to 60W with the Ar pressure constant at 15 mTorr. At a constant 50W of RF power, a similar change in crystallographic structure occurs from predominantly cubic at 40 mTorr to a mixture of cubic and hexagonal at low pressure (10 mTorr).

The optical absorption also changes with sputter power and sputtering gas pressure; see Figure 2.8. The conditions that lead to greater ion bombardment (low pressure or high RF power) produce films with a wider absorption edge or band gap. Much of this upward shift in the band edge probably arises from strain in the films and the change in predominant crystallographic phase. But some shift in band gap may also arise from a composition dependence of the band gap. For cubic films, the dependence of band gap on Mg composition

(x-value) is [1]

$E_g(x) = 1.5 - 0.3x (1-x) + 2x$, where the bowing parameter is 0.3.   **(1)**
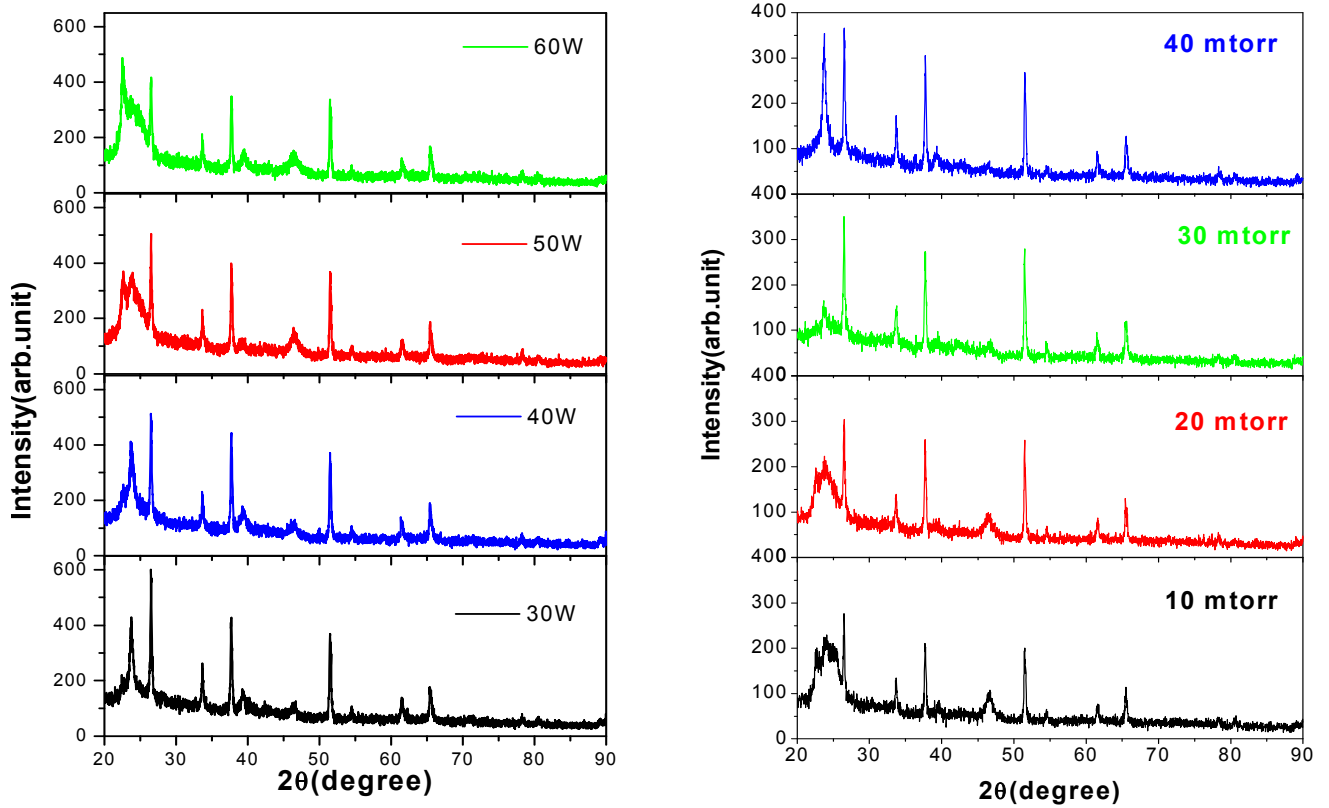
Figure 2.7. XRD spectra of CdMgTe: a) RF power variation b) Ar pressure variation.
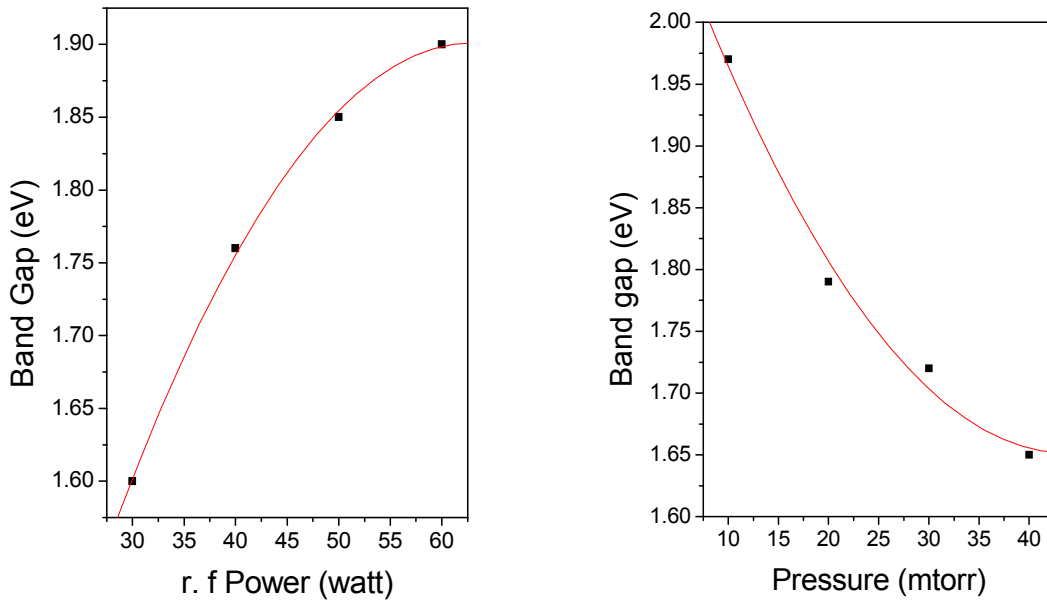
Figure 2.8. Variation of CdMgTe band gap a) vs. RF power at 15 mTorr; b) vs. Ar pressure
          at 50 W of RF power.

Studies were made using atomic force microscopy to estimate the grain size in these films. Consistent with the indications from the x-ray diffraction, the grain sizes ranged from as large as 500 nm at high pressure (40 mTorr) and low RF power (20 W) to as small as 5-10 nm at 20 mTorr and 50 W. In fact the XRD diffractograms of Figure 2.7 show considerable evidence of peak broadening due to small grain size effects.

With respect to the magnetron sputtering of these alloy films of CdMgTe, we find that there is considerable control of the film strain, composition, and crystallographic phase through the sputter parameters of RF power, gas pressure and substrate temperature. One disadvantage of the Mg alloy films is that the sputter rate is noticeably slower than for CdTe or the Mn and Zn alloys. We did find in Phase I that the use of Ne as a sputter gas produced a change in film composition due to the change in mass ratios. Films were slightly richer in Mg content relative to those sputtered with Ar gas. However, the sputter rate was not improved.

2.2   Post-deposition treatments of CdMgTe films

Figure 2.9. Temperature vs. time profile of the one-inch diameter tube furnace. Samples typically spent 2-5 minutes at the treatment time of ~387 $^{\circ}$C.
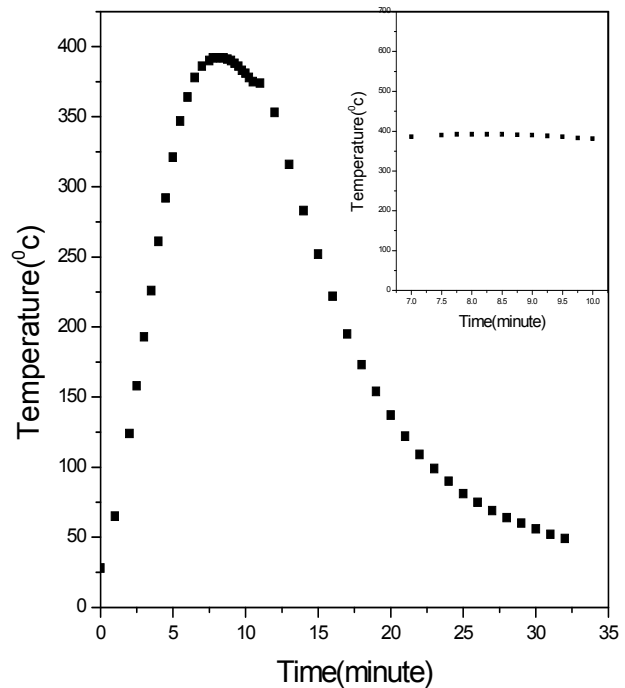
Although alloy films with good optical and crystallographic quality could be produced by magnetron sputtering, we found that CdS/CdMgTe devices exhibited poor photo-response. In much the same way as for CdS/CdTe bilayers, the photo-response could be improved by post-deposition treatments. We used a variety of procedures including annealing in inert ambients and activation treatments in vapors containing chlorine.

Films containing Mg could not tolerate high temperature treatments in vapors containing Cl for longer than a couple of minutes. However, the photovoltaic performance was enhanced by these treatments. Treatments were performed in a small tube furnace with the sample placed face down above a source plate prepared by evaporating several drops of $CdCl_2$/methanol solution on a microscope slide. The film and source plate were separated by ~1mm spacers.

7

After preheating the furnace, the 1 inch diameter quartz tube was placed in the furnace with the sample and source in the tube that had been purged of ambient. Either pure Ar or a dry air flow was maintained through the tub during the high temperature cycle. The time-temperature profile at the sample position is shown in Figure 2.9.

Treatment times longer than about 2 minutes for the samples sputtered from the 40% target (compositions ~20 at% Mg) resulted in considerable shift of the band gap to longer wavelengths (closer to that of CdTe). For the lower composition Mg films, sputtered from the 20% Mg by weight target, treatment times of up to five minutes could be tolerated.

2.3. $Cd_{0.95}Mg_{0.05}Te/CdS$ device

Solar cells with configuration glass/ITO/CdS/$Cd_{1-x}Mg_xTe$/metal were fabricated as described in Sections 2.1 and 2.2. In order to understand the effects of cadmium-chloride activation and Cu diffusion, we have completed devices with and without cadmium-chloride annealing and with and without Cu diffusion. Different devices were made from large-area films which were cut into different pieces. It was found that both cadmium-chloride annealing and Cu diffusion are necessary to obtain better efficiencies. Thus the optimum device fabrication procedure is nearly identical to that of the binary CdTe cells. The effects of vapor cadmium chloride annealing and Cu diffusion on the device parameters are presented in Tables 2.1 and 2.2. Table 2.1 demonstrates that the J_{sc} and hence the device efficiency increases rapidly between 5 and 10 minutes of $CdCl_2$ activation. Further, the required activation duration appears to decrease as the film thickness decreases. All these devices were vapor-chloride treated at 387 ^{o}C and the Cu diffusion time was fixed at 10 minutes at 150°C.

Table 2.1. Device parameters V_{oc}, J_{sc}, FF, and efficiency (η) of $Cd_{0.95}Mg_{0.05}Te/CdS$ top cells vapor-cadmium-chloride treated for different times. Three different deposition plates with different CdTe thickness (d), deposition temperature (T_{sub}) were used. Smaller coupons were cut for differing vapor cadmium chloride activation temperature (T_{CL}), activation duration (t_{CL}), and Cu diffusion time (t_{Cu}).

Device	d (μm)	T_{sub} (^{o}C)	T_{CL} (^{o}C)	t_{CL} (min)	t_{Cu} (min)	V_{oc} (V)	J_{sc} (mAcm^{-2})	FF	η (%)
CGT73a2	0.71	266	387	15	10	.61	11.2	37	2.2
CGT73c1	0.71	266	387	10	10	.63	11.8	37	2.3
CGT73b1	0.71	266	387	5	10	.477	1.40	45	0.2
CGT73b2	0.71	266	387	5	10	.66	3.22	44	0.53
CGT72b1	0.66	250	387	10	10	.65	12.4	32	2.4
CGT72a2	0.66	250	387	5	10	.63	16.2	35	3.4
CGT72b3	0.66	250	387	3	10	.64	9.5	30	1.5
CGT80a1	0.55	250	387	5	10	0.53	9	27	1
CGT80a2	0.55	250	387	2	10	0.43	0.34	30	0.04

Table 2.2 shows the effect of Cu diffusion time on the device parameters. The Cu diffusion temperature was 150 ^{o}C in ambient air. The device performance improves slightly as the Cu diffusion time increases from 5 to 15 minutes.

Table 2.2. The effect of Cu diffusion on the device parameters; V_{oc}, J_{sc}, FF, and efficiency of the $Cd_{0.95}Mg_{0.05}Te$/CdS top cell. Two batches of films were used. Processing conditions are identified as in Table 2.1.

Device	d (μm)	T_{sub} (°C)	T_{CL} (°C)	t_{CL} (min)	t_{Cu} (min)	V_{oc} (V)	J_{sc} (mAcm^{-2})	FF	η (%)
CGT72a1	0.66	250	387	5	5	.64	13.5	33	2.47
CGT72a1-2	0.66	250	387	5	5+10	.65	15	32	2.5
CGT 53	1.75	200	0	0	0	0.38	0.44		
CGT 53	1.75	200	0	0	15	0.37	0.66		

The completed devices were tested under AM1.5 illumination and the I-V characteristic of a typical device under 100 mWcm^{-2} illumination is shown in Figure 2.11. The thickness of the $Cd_{0.95}Mg_{0.05}Te$ film used to fabricate the prototype device was 0.66 μm. The device was annealed at 387 °C for 5 minutes in $CdCl_2$ vapor in dry air. We were unable to fabricate good devices with alloy absorber thicknesses above 1 μm. This is a reflection of the fact that the alloy films have very high resistivity and is consistent with very short minority carrier lifetimes in these films. These factors would explain the poor fill factor and large series resistance.

Figure 2.10. J-V relationship at AM 1.5 illumination (100 mWcm^{-2}) for a prototype $Cd_{0.95}Mg_{0.05}Te$/CdS device.
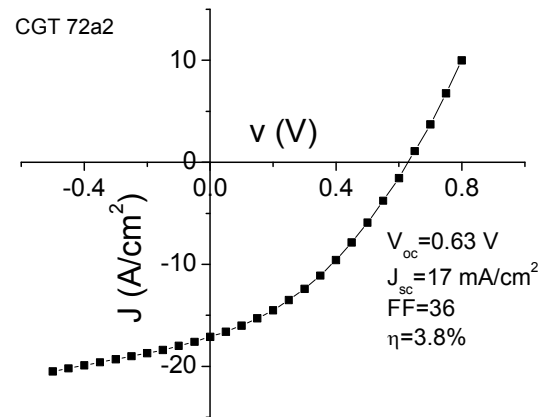
Through collaboration with the University of Nevada Las Vegas group of Clemens Heske, some of the alloy films were studied by x-ray emission spectroscopy. These results are reported in Section 6 below. The results show that these Mg alloy films are highly susceptible to oxidation even prior to chloride activation. However, the activation process in air still results in a significant improvement in the cell performance. Control of oxygen is likely to be very important to further optimization of these alloy films.

One of the important requirements for the top cell in a tandem device is the sub-gap transmittance which controls current matching in a two-terminal device. The transmittance through a $Cd_{0.95}Mg_{0.05}Te$/CdS device (complete except for back contacts) identical to the one used to generate the J-V graph in Figure 2.10 is presented in Figure 2.11. The transmittance spectra were recorded (a) with air as reference, and (b) with a bare Tec-7 substrate as reference. From a comparison of the two spectra it is clear that there is significant transmission loss due to the 3 mm thick Tec-7 substrate (soda-lime glass) with the commercial SnO_2:F. Figure 2.11a

shows about 45 % transmittance through the device structure in the region of interest for a suitable bottom cell. However, the use of more transparent glass and TCO is approximated by spectrum (b) in Figure 2.11, which was recorded with a Tec 7 plate in the reference beam. This shows transmission of about 75% in the relevant spectral region.
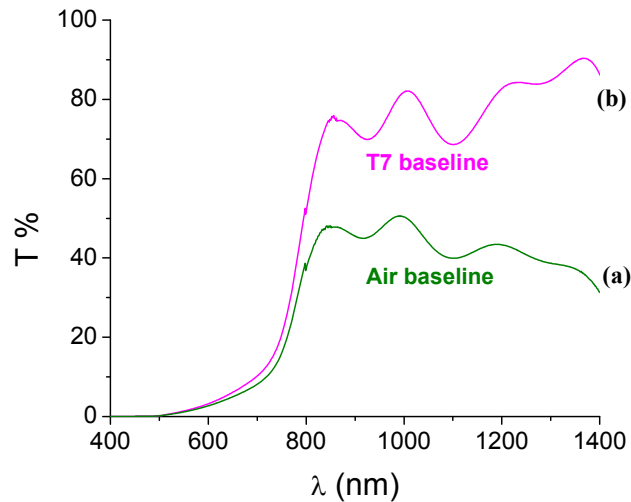
Figure 2.11. Transmittance spectra of a typical Tec7/CdS/ $Cd_{0.95}Mg_{0.05}Te$ device with (a) air as reference, and (b) Tec 7 plate as reference.

2.4. Ultra-thin sputtered CdTe for top cell structures

As an alternative to a wider bandgap II-VI alloy material as a top cell, we studied the performance of cells with ultra-thin CdTe layers, with thickness varying from 240 nm to 870 nm. Tec-15 glass of 3×3 inch was used for this study as substrate. A 65 nm thick CdS layer of uniform thickness was first coated onto the substrate. Based upon our previous studies, thinner CdTe layers require somewhat thinner CdS to obtain optimized cell performance. Our earlier work showed best and average cell efficiencies of 12% and 11%, respectively, with 70nm CdS / 0.95 μm CdTe layers after proper optimization. We have not done this optimization of the CdS thickness in this study. For the purpose of minimizing shunting through CdS, we chose the CdS to be 65 nm.

For the CdTe deposition, we modified the normal geometry by tilting the substrate $45^{°}$ from the normal to the sputter gun, as shown in Figure 2.12. (Previous study has confirmed 1) an approximately linear relationship between film growth rate and distance from the target surface and 2) that the performance of cells made with such angled CdTe deposition also reaches around 12% for 2.3 μm CdTe.) The CdTe film thickness was measured at several positions by stylus profilometry and fitted as a linear function of distance from the edge of thinnest side (Figure 2.13). The CdTe thickness in this set of samples covers the range from 240 nm through 870 nm.

The deposited film area was 54 mm $\times$ 57 mm due to the size of the aperture of the substrate holder and we estimate approximately 2 mm of film was partially shadowed by the edge of the substrate holder on the left and right sides. Thus the film region with slowly varying

thickness is around 50 mm wide. The sample was cut into four 12.5 mm wide pieces for CdCl$_2$ treatment with different durations, as recorded in Figure 2.13. After all the CdCl$_2$ treatments, the four pieces were put together for a single 15Å Cu/ 200 Å Au back contact evaporation followed by a12.5 minute thermal contact activation at 150 $^{\circ}$C in ambient air. After the contact activation, laser scribing was employed to define square cells with 3mm × 3mm dimensions. The laser scribing defined 19 cells per row with the same CdTe thickness. The average efficiency of cells that had efficiency at least 50% of the best of the 19 cells of each row is plotted in Figure 2.14, together with those best cells. Cells below this threshold were excluded from the calculation.
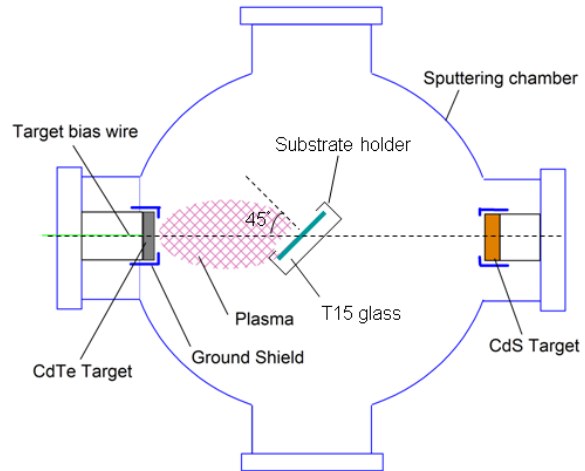
Figure 2.12 Top view of sputtering chamber using tilted CdTe deposition at 45°.
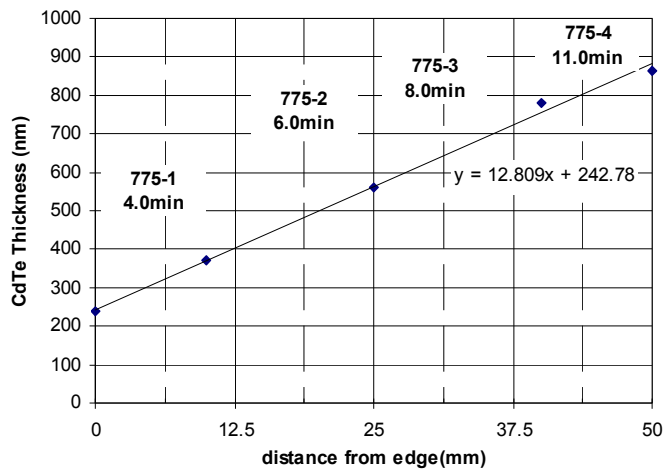
Figure 2.13 CdTe film thickness vs distance from the edge of thinner side.

The most interesting result of these cells is that the best performance of 330 nm CdTe reaches 6.0% with Jsc of 19.55 mA/cm^2. The average efficiency of these 330 nm thick cells is 4.9%, although the yield was only 31%. For the thinnest CdTe film (240 nm), the best efficiency can also reach 5.2% with Jsc of 17.5 mA/cm^2 and 37% yield. The QE of the best cells with CdTe below 450 nm is plotted in Figure 2.15. The data from this single, preliminary study indicate a gradual trend of decreasing performance but probably no fundamental limit to the

fabrication of ultra-thin CdTe cells that yield a current-matching condition for two-terminal tandem devices.

Figure 2.14 Average and best cell performance as function of CdTe film thickness.
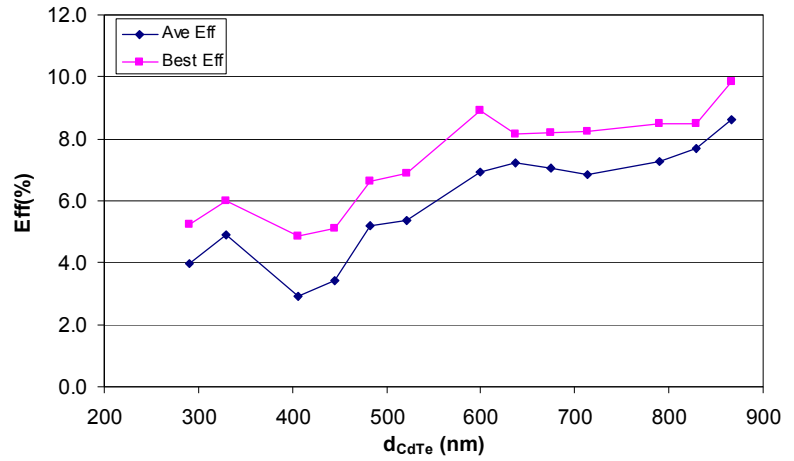
Figure 2.15 Quantum efficiency of cells with CdTe thickness below 450 nm.
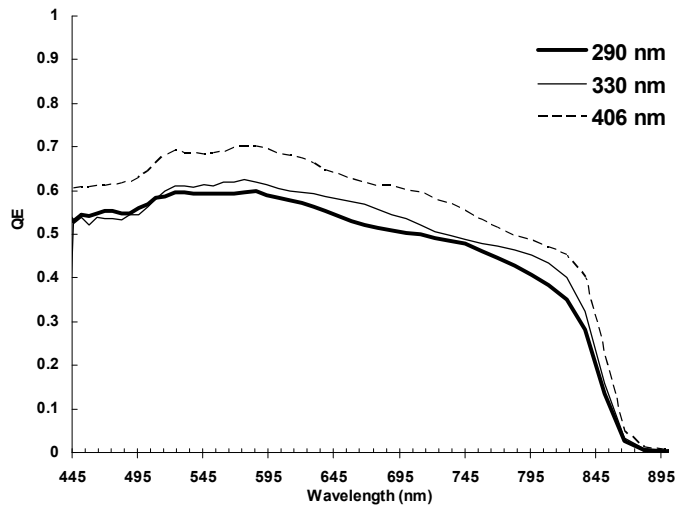
3. Transparent Contacts/Window Layers and Recombination Junctions (Task 12)

Transparent back contacts to top cells are particularly useful if the contact is a p+/n+ structure for then it would be identical to a recombination junction in a monolithically integrated double-junction tandem cell. Thus it is possible to make a single-junction cell with transparent back contact that is the top half of a tandem and optimize this top half separately.

Thus, we studied CdS/CdTe solar cells with 2.3 μm CdTe thickness on which we prepared four different types of p+/n+ transparent back contacts (TBCs). We used ZnTe:Cu and ZnTe:N as the p-type materials, and ZnO:Al and indium tin oxide (ITO) as the n-type materials. This gives four possible combinations: ZnTe:Cu/ZnO:Al, ZnTe:N/ZnO:Al, ZnTe:Cu/ITO, and ZnTe:N/ITO. Our results show that ZnTe:N/ITO gives the best results. This back contact was then used to make cells of reduced (1.8 μm and 0.7 μm) CdTe thickness with the best cells giving performance up to 9.1% efficiency.

All cells were prepared on commercially available Pilkington TEC 7 fluorine-doped tin-oxide-coated soda-lime glass. All subsequent layers were deposited by RF sputtering in pure argon except for the ZnTe:N which was reactively sputtered in ~5% N_2 in argon. CdS and CdTe were deposited at 250°C and 18 mTorr argon pressure with 35 and 20 watts of RF power, respectively into the two-inch magnetrons. All samples used nominally the same 0.13 μm thickness of CdS. After CdS/CdTe deposition, the 2.3 μm CdTe samples were $CdCl_2$ treated at 387°C for 30 minutes. Samples having CdTe with reduced thickness were treated for a time reduced in proportion to their thickness. After $CdCl_2$ treatment, the next layer was either ZnTe:N deposited from an undoped ZnTe target by reactive sputtering in a 5% nitrogen-95% argon environment, or ZnTe:Cu deposited from a target doped with 2% copper by weight. In both cases, the layer was deposited at a substrate temperature of 325°C. The final layer was an n-type transparent conductive oxide, either ITO or ZnO:Al. The ITO target was 90% In_2O_3 and 10% SnO_2 by weight. For the ZnTe:Cu/ITO contact, ITO was deposited at 150°C. For the ZnTe:N/ITO contact, ITO was deposited at various temperatures. The ZnO:Al was deposited at 200°C from a ceramic target with 2% Al_2O_3 by weight.

When ITO was used as the final n+ layer, we found that the resistivity of the film needed to be controlled carefully to obtain good cell performance. The following section describes the variation in ITO conductivity with deposition conditions during RF sputtering.

3.1 Effect of ITO Deposition Temperature

Figure 3.1 shows that the conductivity of ITO deposited on glass can be controlled over three orders of magnitude as the substrate temperature increases from 25 °C to 300 °C.
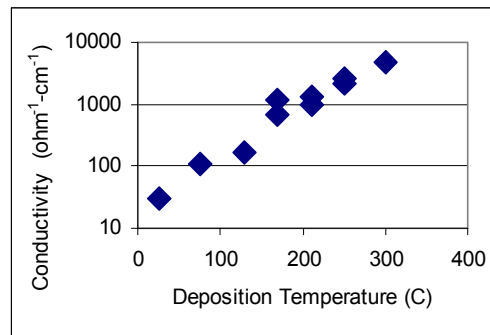
Figure 3.1 Variation of ITO conductivity with deposition temperature.

13

Although one might expect the best solar cells to use transparent back contacts with the greatest conductivity, we have observed that this is not necessarily the case. Figure 3.2 shows J-V curves obtained from three cells with 2.3 μm CdTe and a ZnTe:N/ITO back contact for various ITO deposition temperatures. For low deposition temperature (50°C) ITO (figure 3.2a), the open-circuit voltage is similar to the middle and high temperature cases (Figures. 3.2b and 3.2c), but efficiency is limited by large series resistance, lowering the short-circuit current and reducing the fill factor essentially to 25%. In the case of medium temperature deposition (170°C), good overall parameters are obtained (Figure 3.2b). When the temperature is increased further to 300°C (Figure 3.2c), the performance is pathological. "Rollunder" appears in the fourth quadrant that reduces the fill factor to less than 25%. Such cells also usually have higher efficiency when illuminated from the back side than from the front.

We believe this problem observed at high temperature is not due to subjecting the entire cell to high temperature in the final stage of the deposition, for the following reasons. The previous deposition of ZnTe:N in this contact structure is done at even higher temperature (325°C). It is possible to measure J-V curves by contacting the ZnTe:N adjacent to the ITO contacts, and while current collection is very poor, no rollunder or rollover is observed. (The ZnTe:N is not deposited through a mask but forms a continuous film on the CdTe.) Finally, it is possible to first deposit dot cell ITO contacts at the high temperature condition and then perform a second deposition of dot cell contacts at the medium temperature condition between the high temperature ITO contacts, and the behavior of the different series of cells is what would be obtained with a single deposition. We speculate that the development of rollunder is caused by poor band alignment between the ZnTe:N and the high-temperature deposited ITO, as the electron affinity of ITO may change with preparation conditions.
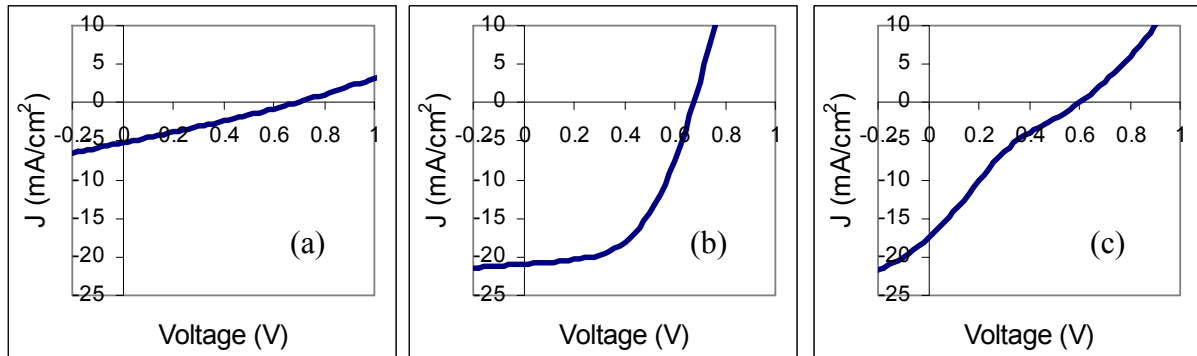
Figure 3.2 J-V curves of CdTe/ZnTe:N/ITO cells using (a) low temperature and low conductivity, (b) medium temperature and medium conductivity, and (c) high temperature and high conductivity ITO.

3.2   Performance of 2.3 μm Cells with Different Back Contacts

Figure 3.3a shows the J-V curves for cells with ZnO:Al as the n-type contact. Of the four types of contacts used in our study, ZnTe:N/ZnO:Al gives the worst performance, with open circuit voltage being particularly poor. While the ZnTe:Cu/ZnO:Al contact has a reasonable open circuit voltage, typical of CdTe cells containing copper, the large series resistance (23 ohm-cm^2) decreases the fill factor, which is the greatest limitation to its the efficiency as compared to ZnTe:N/ITO cells. Figure 3.3b shows the J-V curves for cells with ITO as the n-type contact.

For cells with ZnTe:Cu as the p-type layer, the most dramatic difference here from the cells with ZnO:Al is the rollover in the first quadrant in the ITO case. This is typical of a back contact barrier that can result from poor valence band alignment at the back contact.   Of the four types of contacts, ZnTe:N/ITO gives the best overall results, provided the ITO conductivity is optimized through the appropriate deposition temperature.

The parameters and performances of the best cells with each back contact and for 2.3 μm of CdTe are summarized in Table 3.1. In addition, we present the results of the optimized transparent contact on cells with thinner CdTe.
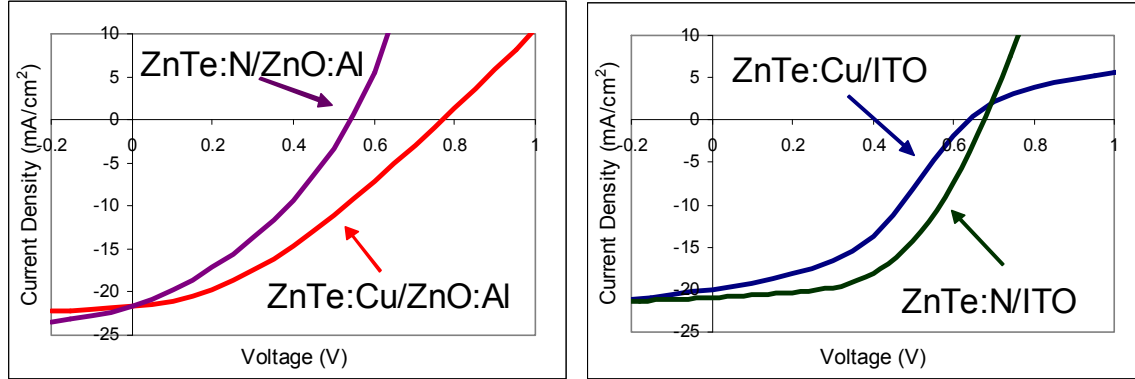
Figure 3.3 J-V data for cells with 2.3 μm CdTe (a) with ZnO:Al as the n-type layer (b) with ITO as the n-type layer.

Table 3.1 Efficiency and second-order metrics for CdTe cells with transparent contacts.

Back Contact	CdTe thickness (μm)	Voc (mV)	Jsc (mA/cm^2)	Fill Factor (%)	Efficiency (%)
ZnTe:Cu/ZnO:Al	2.3	762	20.8	38	6.1
ZnTe:Cu/ITO	2.3	640	17.7	43	4.9
ZnTe:N/ZnO:Al	2.3	543	21.6	35	4.1
ZnTe:N/ITO	2.3	676	21	53	7.5
ZnTe:N/ITO	1.8	643	19.9	65.1	9.1
ZnTe:N/ITO	0.7	676	21.7	52.4	7.4

3.3   Cells with ZnTe:N/ITO Back Contact and reduced CdTe thickness

Although our standard CdTe cells with metal back contacts use 2.3 μm of CdTe, such thicknesses are unlikely to be useful in double-junction cells. In monolithically integrated cells, the currents produced by the top and bottom cells must be equal. This current-matching condition is easier to meet if the top cell is more transparent, and in fact thinner CdTe can transmit an appreciable fraction of above-bandgap light. Furthermore, we have shown that it is possible to fabricate cells with metal contacts and as little as 0.7 μm of CdTe and achieve reasonable performance [2] comparing favorably to our best CdTe cells.[3]

With that motivation, we have fabricated cells of different CdTe thicknesses using the ZnTe:N/ITO contact found to be best for 2.3μm CdTe cells. The last three rows of Table 3.1

summarize the best cell performances as a function of CdTe thickness for the optimized, transparent contact.

Among the back contacts tested in our study, ZnTe:N/ITO is found to give the best results. Our best cell with an n-type/p-type bilayer back contact is 9.1%. There is plenty of room for improvement compared to our best cell on the same Tec-7 substrate with a metal back contact, which is 12.6%, but we are optimistic that further improvements will be possible. Future work will involve other back contact optimizations, including attempts at incorporating copper or a tellurium-rich layer. Measurements and modeling are also needed to understand band alignment issues, carrier lifetimes, depletion widths and neutral regions.

4. *Interconnect studies and related nonideal tandem cell modeling (Task 13)*
4.1. Optical Modeling of II-VI Tandem Device Performance
4.1.1 Introduction

Three separate experimental approaches have been adopted for application of spectroscopic ellipsometry to alloy materials and device development.

(1) Ex situ ellipsometric spectra are obtained on as-deposited films to determine the band gap and critical point structure (i.e., the higher energy band gaps). Such measurements are can also be repeated after post-deposition treatments (such as annealing in $CdCl_2$ vapor) and the energy shifts and changes in width of the band gap and critical point structures provide information on the survivability and ultimately improvement of the alloy. Such results were presented in Sec. 6.1.

(2) Accurate dielectric functions are determined for those alloys that have been deposited and successfully treated post-deposition while retaining the appropriate alloy composition and band gap. Dielectric functions are also determined for all other components of the device, including the glass and TEC coatings [4], the window layer, transparent back contact, and recombination junction materials, and the metal contacts.

(3) The dielectric function database is then used in the optical design of tandems, focusing on the two terminal configuration that requires current matching. In such studies, the maximum possible current is determined, based on incident AM 1.5 irradiance. In addition, the absorption within the superstrate glass, the TEC coatings, window layer, transparent back contact, and recombination junction materials provide insights into the practical limitations on the photon collection capability of the tandems.

4.1.2 Results and Discussion
4.1.2.1 Optical Properties of II-VI Tandem Cell Components

Dielectric functions determined as described in Sec. 1 were used for the active layer alloy components. For the near band edge optical properties, the index of refraction was used from spectroscopic ellipsometry (SE) measurements, whereas the absorption coefficient was used based on SE but with an extrapolation just above the band gap given by $\alpha(E)n(E)E = B(E - E_g)^{1/2}$, as would be expected from a direct band gap semiconductor. This helps to ensure that the determined quantum efficiency reflects high quality, active thin film materials.
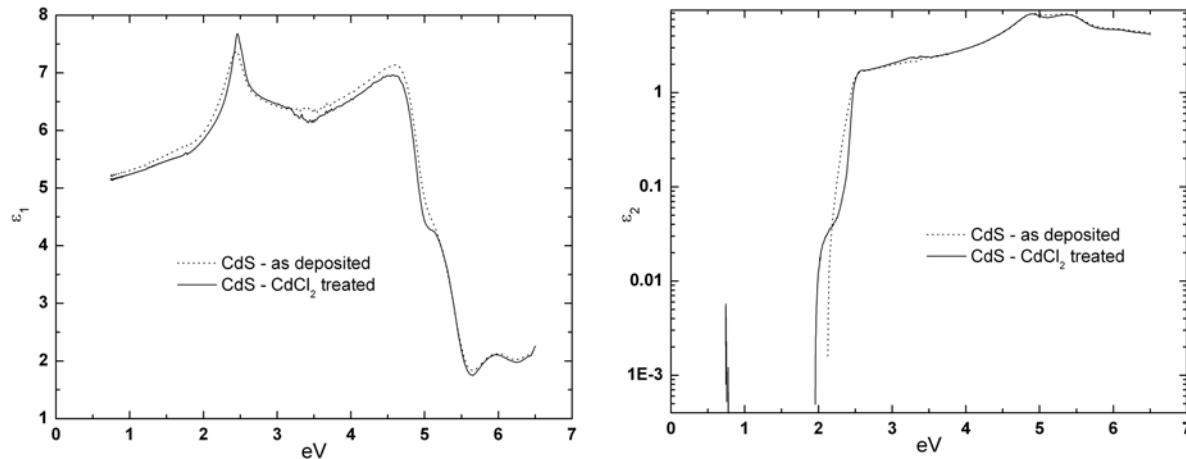

Figure 4.1 Dielectric function of as-deposited and $CdCl_2$ treated CdS, the latter used in optical modeling of tandem solar cell performance.

Figure 4.1 shows an example of the determination of the optical properties of the other components of the device. In this case, the CdS results shown were obtained on a film deposited on fused silica with a substrate temperature of 250°C, at an Ar pressure of 18 mTorr, and 35 W RF power. The time of deposition is 8.5 min, which leads to a film with a bulk layer thickness of d_b = 1230 Å. A two-layer roughness/bulk optical model was used, and the surface roughness thickness as an effective medium layer was found to be d_s = 43 Å. Thus, the effective thickness (d_b + 0.5d_s) deposition rate was 2.5 Å/s. Only SE data are used to extract the optical properties for this film; for thicker films, transmission data are also used in order to find obtain more accurate values of ε_2 just above the band gap.
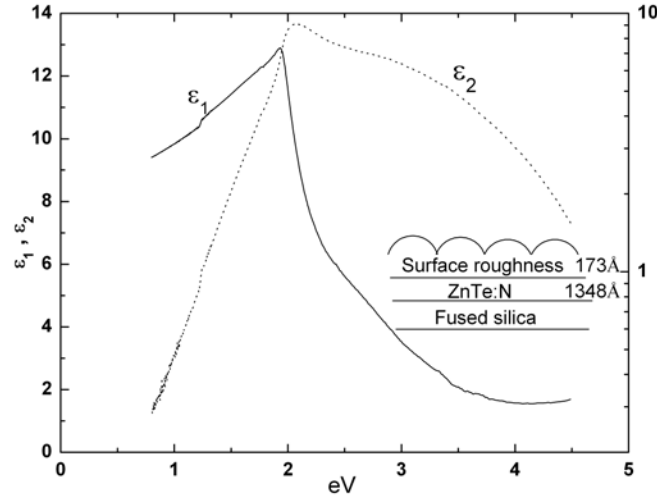
Figure 4.2 Dielectric function of ZnTe:N fabricated by RF magnetron sputtering of a ZnTe target using gas flows of ~ 2 sccm of N_2 and ~ 60 sccm of Ar.

Figures 4.2 and 4.3 show dielectric functions for two types of p-type doped transparent back contact materials prepared by rf magnetron sputtering [5]. These data provide a basic understanding of the nature of the materials and their absorption characteristics. The material intended to be ZnTe:N shown in Figure 4.2 was deposited from a pure ZnTe target onto fused silica held at 325°C. The gas pressure was 10 mTorr, the gas flows consisted of ~ 2 sccm of N_2 and ~ 60 sccm of Ar, and the RF power was 80 W, leading to a deposition rate of 2.4 Å/s. For this p$^+$-type back contact material, no evidence of crystalline ZnTe structure appears. The results suggest that the N_2 plays a key role in the sputtering process, altering the crystalline structure of the material, possibly leading to a-Te inclusions. In fact, with the exception of sharp features in (ε_1, ε_2) near 2 eV, the material appears amorphous. For ZnTe:Cu shown in Figure 4.3, no N_2 was used and the Cu was introduced through the target (0.75 wt.% Cu). For the ZnTe:Cu, the three higher energy critical points in Figure 4.3 at 3.61, 4.15, and 5.26 eV mirror those in single crystal ZnTe, but are much broader. The band gap critical point in the thin film could not be detected and instead broad band edge absorption appears as an effect of the heavy Cu doping. Thus, the results of Figures 4.2 and 4.3 for the two different p-type ZnTe films demonstrate how a routine ex situ optical measurement can provide insights into the nature of new materials.

Finally, Figure 4.4 shows the dielectric function of a sputtered In_2O_3:Sn thin film that is designed for use as a transparent interconnect between polycrystalline top II-VI alloy and bottom cells. The substrate temperature was 95°C, the gas pressure and flow were 4.7 mTorr and 30

sccm, respectively, the RF power was 60 W, and the deposition time was 15 min. These results were obtained by combining ex situ spectroscopic ellipsometry and transmission spectroscopy in order to characterize the weak absorption, particularly at low energy where absorption losses are undesirable. Here a very clear free electron absorption tail is observed below 1.5 eV in both parts of the dielectric function.
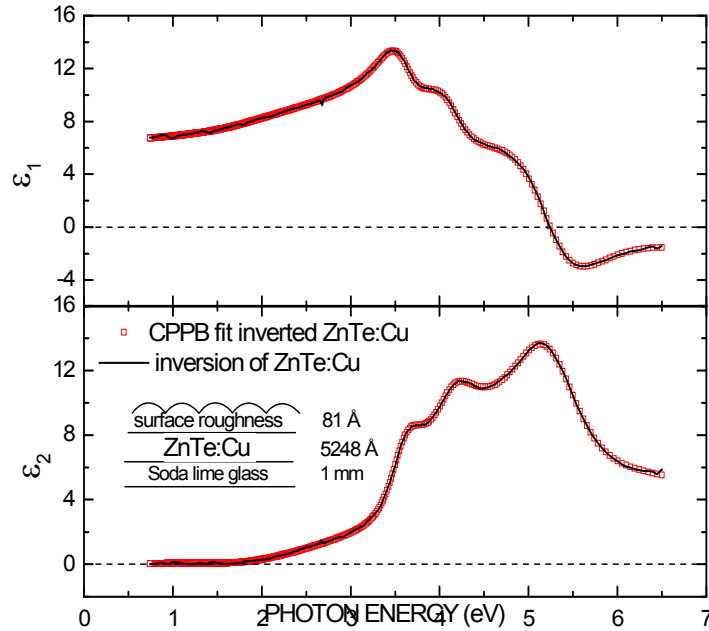

Figure 4.3. Dielectric function of ZnTe:Cu fabricated by rf magnetron sputtering of a ZnTe target incorporating 0.75 wt.% Cu.
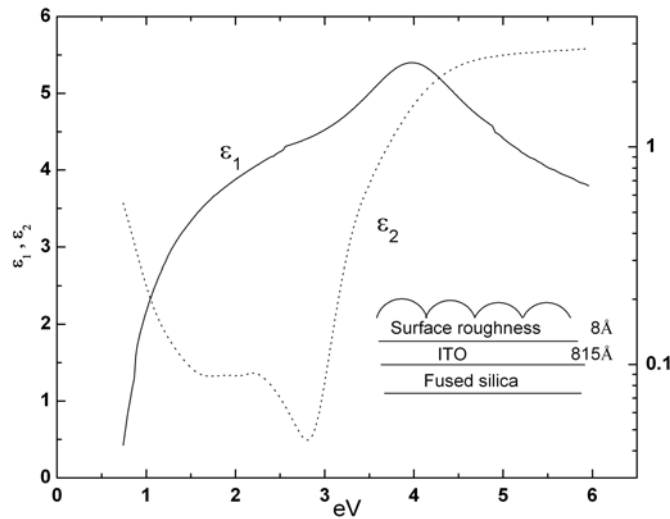

Figure 4.4. Optical constants of In_2O_3:Sn used as a transparent interconnect for II-VI tandem solar cells.

4.1.2.2   Optical Modeling of II-VI Tandem Solar Cells

Figure 4.5 shows the short circuit current under current-matching conditions as a function of total active layer thickness for hypothetical $Cd_{1-x}Mg_xTe$ - $Hg_xCd_{1-x}Te$ tandem solar cell structures.

The individual layer thicknesses are given at the right side of Figure 4.5 with the active layer thicknesses, varied so as to achieve current matching as given in Table 4.1. Dielectric functions for the best $Cd_{1-x}Mg_xTe$ with a band gap of 1.6 eV were used, as were those for $Hg_xCd_{1-x}Te$ with a band gap of 1.1 eV. For $Hg_xCd_{1-x}Te$, development of improved dielectric functions for the optimum treated films is in progress.

Soda lime glass	3mm
SnO₂	350 Å
SiO₂	214 Å
SnO₂:F	3490 Å
CdS	1300 Å
Cd₁₋ₓMgₓTe (1.6 eV)	X Å
ZnTe:(Cu or N)	1000 Å
In₂O₃:Sn	1000 Å
CdS	1300 Å
HgₓCd₁₋ₓTe (1.1eV)	Y Å
Cu	30 Å
Au	200 Å
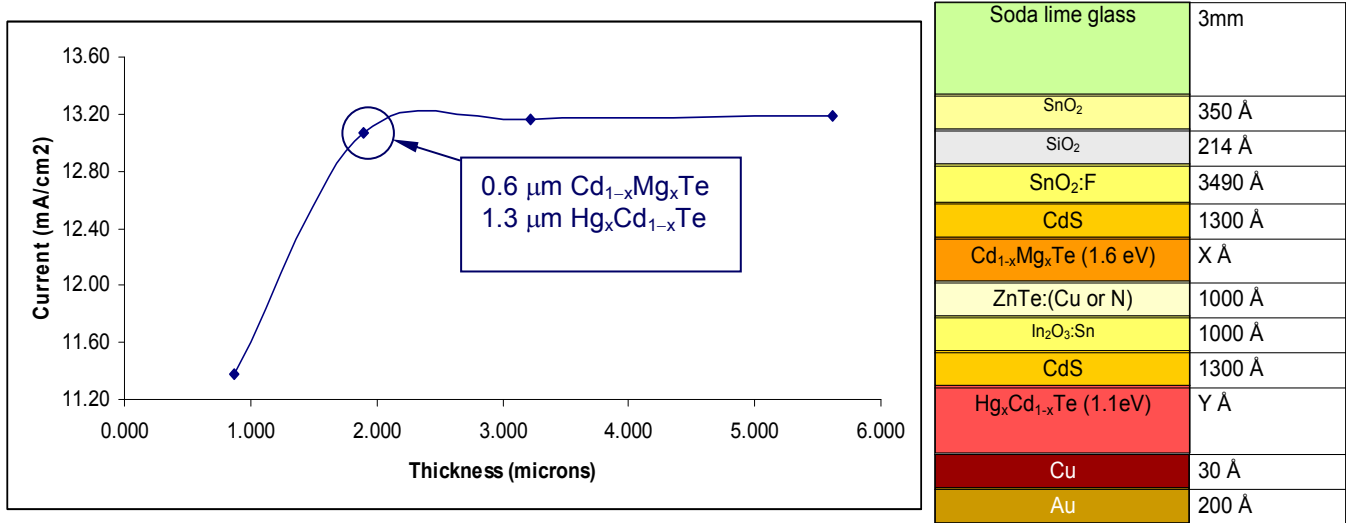
Figure 4.5 Short circuit current under current matching conditions versus total active layer thickness (X+Y) predicted for a tandem II-VI solar cell based on thin film optical modeling. The tandem stack and other layer thicknesses are shown at the right.

Table 4.1. Thickness of active layers and short circuit current under current matching conditions obtained from optical modeling of tandem II-VI PV devices.

Thickness of active layers (µm)			Short circuit current
$Cd_{1-x}Mg_xTe$	$Hg_xCd_{1-x}Te$	$Cd_{1-x}Mg_xTe + Hg_xCd_{1-x}Te$	(mA/cm^2)
0.440	0.435	0.875	11.38
0.600	1.300	1.900	13.07
0.615	2.600	3.215	13.16
0.615	5.000	5.615	13.19

Figure 4.6 shows the results of the calculations of optical quantum efficiency and reflectance, and Figure 4.7 includes absorption losses in the non-active layers for the pair of current-matched thicknesses of 0.6 µm for $Cd_{1-x}Mg_xTe$ and 1.3 µm for $Hg_xCd_{1-x}Te$. The optical model enables one to evaluate the origin of the losses in a realistic structure designed for low cost, including, for example, a soda-lime glass substrate with TEC-15 coatings as in current CdTe module production. The losses that arise from the reflectance and absorbance in Figures 4.6 and 4.7 have been evaluated in terms of lost current.

(i) Reflection from the full structure amounts to 1.9 mA/cm^2 for $E > 1.6$ eV and 3.7 mA/cm^2 for $1.1 < E < 1.6$ eV. These losses can be reduced through antireflection coatings on the top glass as well as improved anti-reflection characteristics, first between the TEC-15 layers and the top cell, and second between the interconnect layer and the bottom cell. The latter reflection is particularly significant.
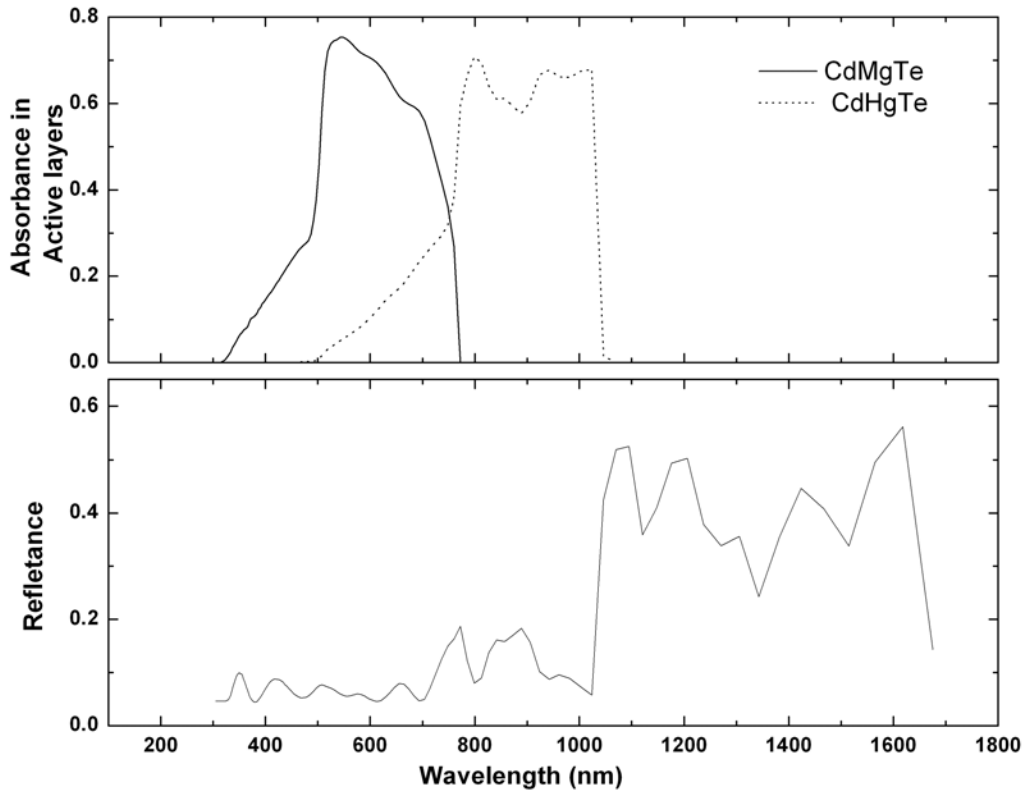
Figure 4.6. Predicted optical QE and reflectance for a Cd$_{1-x}$Mg$_x$Te (0.6 μm) - Hg$_x$Cd$_{1-x}$Te (1.3 μm) tandem.

(ii) Absorption in the soda-lime glass and TCO layers using the optical stack and layer optical properties appropriate for TEC-15 amounts to 2.3 mA/cm^2 for $E > 1.6$ eV and to 4.1 mA/cm^2 for $1.1 < E < 1.6$ eV). The absorption of soda-lime glass in the infrared seems to generate the primary problem for the bottom cell, and the absorption by the SnO$_2$:F generates the problem for the top cell.

(iii) Absorption in the top 1300 Å CdS layer amounts to 4.9 mA/cm^2 for $E > 1.6$ eV. This layer does not affect the bottom cell collection, nor does the CdS window layer of the bottom cell affect this collection.

(iv) Absorption in the heavily doped 1000 Å ZnTe:Cu top cell back contact amounts to 1.0 mA/cm^2. This is due to a relatively strong absorption tail below the band gap, most likely due to heavy doping as can be seen in Figure 4.3. Figure 4.8 shows how the quantum efficiency component from the bottom cell can be enhanced when the thickness of the ZnTe:Cu is reduced to 400 Å. When the ZnTe:N is used, the absorption is so strong that the thickness of layer must be reduced from 1000 Å to 400 Å and even then, current matching is only possible at the level of 9.6 mA/cm^2 due to limited current collection in the bottom cell.
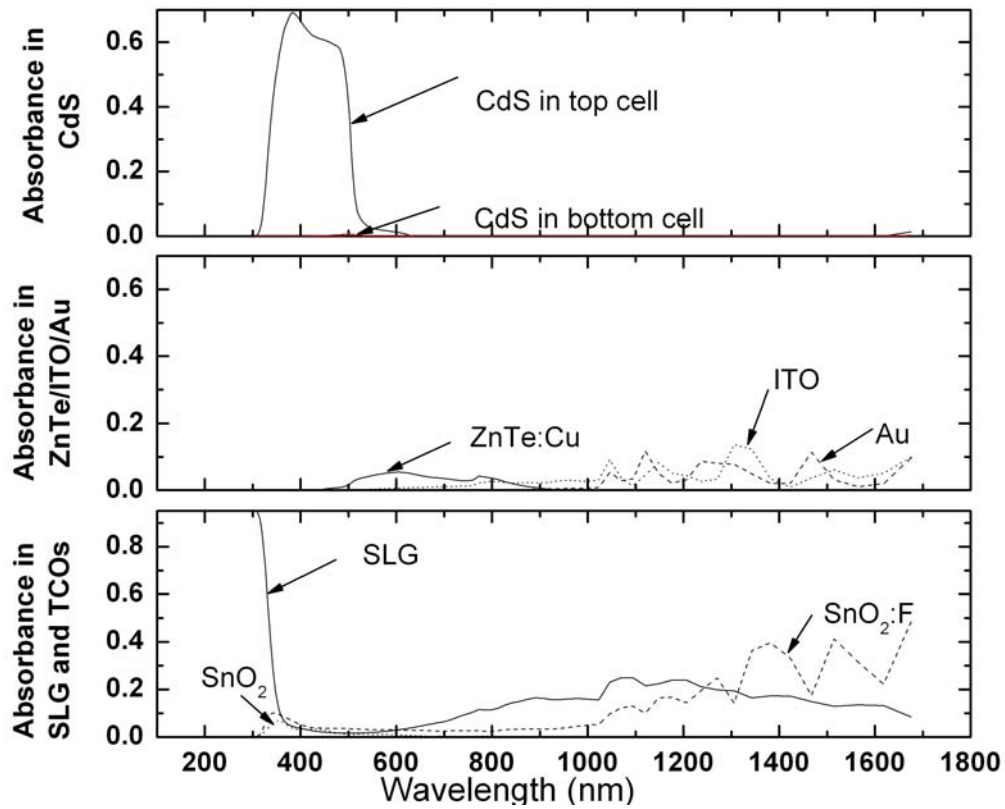
Figure 4.7. Predicted absorbances in the substrate and non-active layers for a $Cd_{1-x}Mg_xTe$ (0.6 μm) - $Hg_xCd_{1-x}Te$ (1.3 μm) tandem.
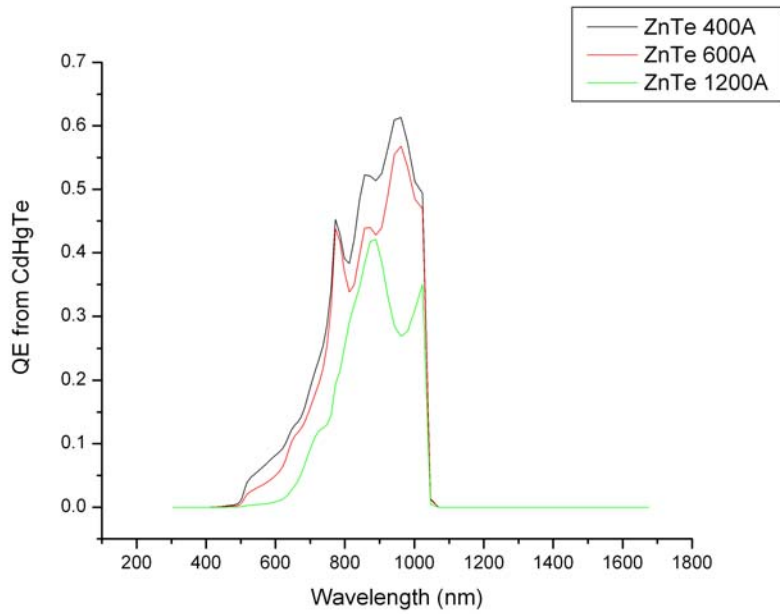
Figure 4.8. Improvement of the quantum efficiency of the $Hg_xCd_{1-x}Te$ bottom cell due to a reduction in the top cell ZnTe:Cu transparent back-contact thickness.

Considering these optical losses, if a cell could be made with a V_{oc} of 1.5 V and a fill factor (FF) of 0.75, the current of 13.1 mA/cm^2 would yield an efficiency of ~14.7%. The losses described above are well-balanced between the top cell (9.1 mA/cm^2) and bottom cell (8.8 mA/cm^2), however, and if these losses could be overcome, the matched current could reach ~22 mA/cm^2. The above V_{oc} and FF would then yield 24.6% efficiency. Thus, such modeling gives insights into the specific optical issues that must be overcome to reach high efficiencies in polycrystalline thin film tandem PV technology.

4.1.3 Conclusion

The utility of optical studies based on spectroscopic ellipsometry for development of thin film II-VI ternary alloys for tandem PV has been demonstrated. The dielectric function of the films in as-deposited and CdCl$_2$ treated states provide immediate feedback into the success of the treatment. Also, the dielectric functions of all the components of the tandem device serve as a database for tandem cell optical design.

5. HgCdTe bottom cell studies/back contact (Task 14)

Sputter deposition of Hg alloys of CdTe has continued in Phase III of this project. It was found in Phase II that the substrate deposition temperature had a strong effect on the Hg concentration in the film. Thus considerable effort was placed on obtaining a reliable measurement of the substrate temperature which is radiatively heated from a tantalum wire heater approximately 2 cm behind the substrate. Thermocouple probes on the front and back sides of the glass substrate showed large differences in readouts unless they were bonded to the glass with indium solder. However bonding the thermocouple tips is not convenient as a standard practice. Concurrently we used optical interference fringes from the front and back sides of the glass as reported in earlier work. Once the temperature was calibrated, we found that heater power was a reliable indicator of substrate temperature as long as the substrate was a glass coated with a TCO opposite the heater. The difference in absorptivity and emissivity of the two surfaces – glass and TCO has a large effect on the substrate temperature.

Figure 5.1 J-V curves of two small dot cells with HgCdTe absorber layers as indicated.

Legend:
- mct86V.16
- mct86V.17
- mct78F08

MCT86V = T7/ CdS(0.1um)/ CdTe(0.2um)/HgCdTe (~1.5 um) + CdCl2 treatment (420 °C, 2 min)

MCT86V (Dot 17)
Voc = 503 mV
Jsc = 24.5 mA/cm2
FF = 54.3 %
Eff = 6.7 %
Area = 0.031 cm2

MCT86V (Dot 16)
Voc = 507 mV
Jsc = 24.6 mA/cm2
FF = 50.0 %
Eff = 6.2 %
Area = 0.031 cm2

MCT78F = T7/ CdS(0.2 um)/HgCdTe (~1.5 um) + CdCl2 treatment (420 °C, 2 min)

MCT78F (Dot 08)
Voc = 386 mV
Jsc = 17.9 mA/cm2
FF = 49.6 %
Eff = 3.4 %
Area = 0.031 cm2

Axis labels: Current Density (A/cm^2) vs Voltage (V)

5.1 HgCdTe cell fabrication

The sputter deposition temperature was optimized to 85 °C. A series of cells were prepared with junctions of CdS/HgCdTe in order to make a preliminary optimization of the deposition conditions. This was followed by the addition of a pure CdTe interfacial layer next to the CdS window layer. These cells yielded the best J-V response (Figure 5.1). The external quantum efficiency (Figure 5.2) shows that there is substantial photocurrent response out to a wavelength of 1100 nm. This is consistent with an absorber composition having a Hg content of 15%.

5.2 Back contacts for the bottom cell

For cells prepared with the Hg-alloy absorber, we found that an evaporated Cu/Au back contact similar to that used for the pure CdTe absorber cells gave good performance and no further work was done on the back contacts.

Figure 5.2 External quantum efficiency of the two cells of Figure 5.1. No light or voltage bias was used.
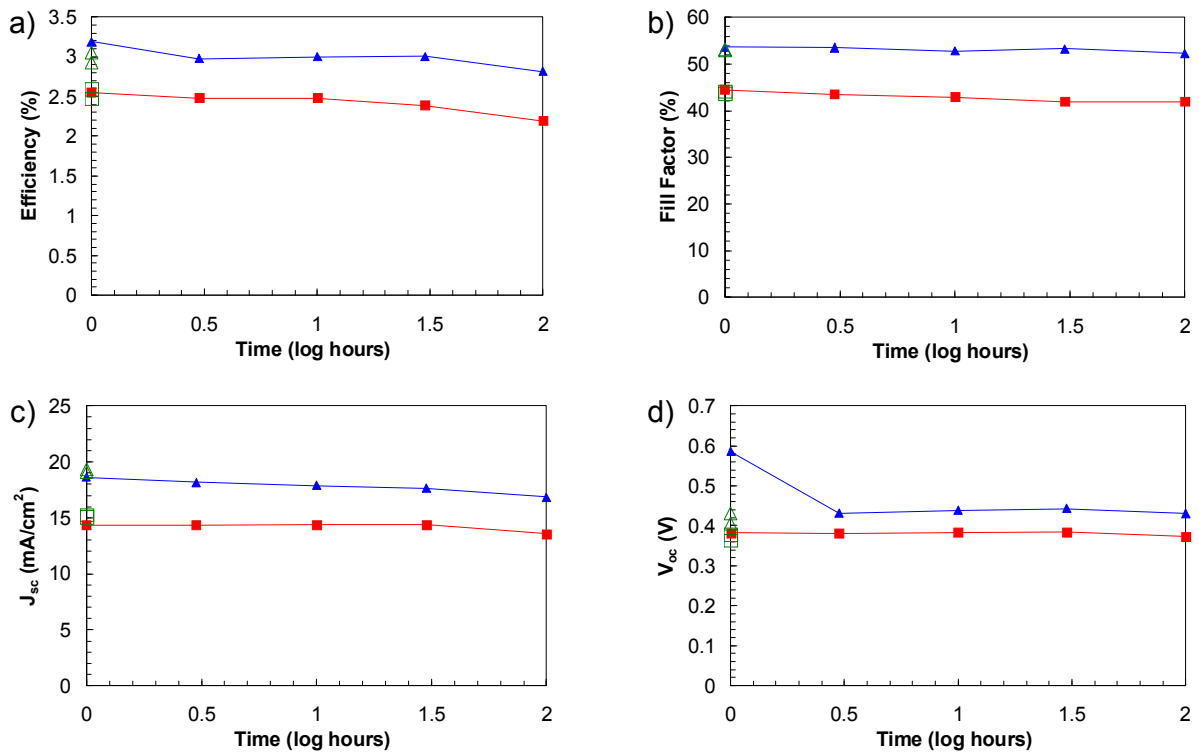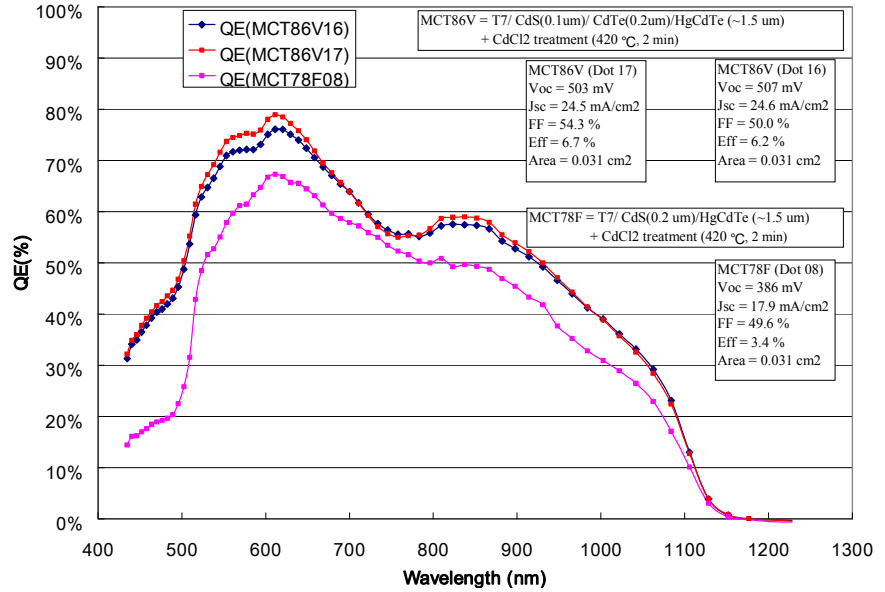
Figure 5.3. Results of light soaking HgCdTe cells. (a) Efficiency (%); (b) FF (%); (c) J_{SC} (mA/cm^2); and (d) V_{OC} (V). For each plot, the median values (solid red square) and best value (solid blue triangle) are shown. On the ordinate are the initial measurements (green, hollow). A sample size of 60 cells with area of 0.031cm^2 was used. A minimal loss of efficiency of only 0.3% over 100 hour period is shown.

5.3 Light soak stressing of CdHgTe

The results of light soak stressing of CdHgTe cells are shown in Figure 5.3. These cells were MCT80E and MCT80b Tec7/CdS (100 nm)/CdHgTe(1.3 μm)/Cu(3 nm)/Au(20 nm) with a $CdCl_2$ activation treatment of 4 min at 430°C. Since cells with reasonable efficiency were only achieved in the last quarter, this work was done on cells fabricated with a maximum efficiency of 3.25% and no encapsulation. The data indicate very good stability considering that the cells are not encapsulated. Of particular note is the fact that the V_{OC} is constant while the degradation comes mostly from the drop in J_{sc}.

6. *Characterization and Stress Studies (Task 15)*

6.1 Real Time Spectroscopic Ellipsometry Studies of II-VI Alloy Films

6.1.1 Introduction

Spectroscopic ellipsometry is an excellent non-contacting technique for investigating thin-film optical properties, electronic structure, and surface microstructure. This technique has been applied for materials evaluation in order to explore the opportunities and identify the potential difficulties in the fabrication of II-VI materials for top cells in two-junction devices with either monolithic two-terminal or mechanically stacked four-terminal structures (see Figure 6.1). In this research, two types of top cell material, $Cd_{1-x}Mn_xTe$ and $Cd_{1-x}Mg_xTe$ have been studied for their suitability in tandem PV devices with a $Hg_xCd_{1-x}Te$ bottom cell.

glass
ZnO
CdS
$Cd_{1-x}Mg_xTe$
ZnTe
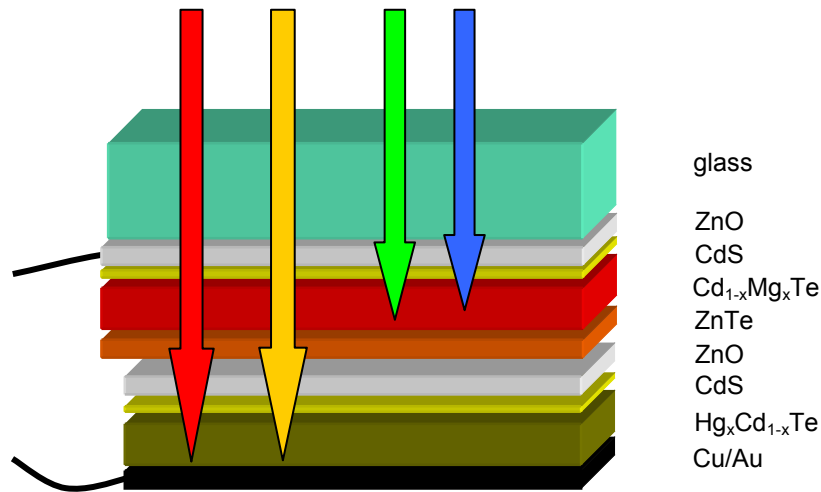ZnO
CdS
$Hg_xCd_{1-x}Te$
Cu/Au

Figure 6.1. Two-terminal tandem cell based on $Cd_{1-x}Mg_xTe$ and $Hg_xCd_{1-x}Te$ absorbers.

6.1.2 Top cell material candidates: $Cd_{1-x}Mn_xTe$ and $Cd_{1-x}Mg_xTe$

6.1.2.1 $Cd_{1-x}Mn_xTe$ and $Cd_{1-x}Mg_xTe$ preparation

$Cd_{1-x}Mn_xTe$ films were magnetron sputtered on soda-lime glass substrates from a target composed of 13 weight % MnTe and 87 weight % CdTe. $Cd_{1-x}Mg_xTe$ films were magnetron sputtered on soda-lime glass from a commercially-fabricated target composed of 20 weight % MgTe and 80 weight % CdTe. A first estimate of the composition of the as-deposited alloys films was made on the basis of the optical absorption edge determined from the transmission spectra. The $Cd_{1-x}Mn_xTe$ film thickness was typically about 1 μm; $Cd_{1-x}Mg_xTe$ films were thinner -- about 0.2 μm. A $CdCl_2$ post-treatment was performed as an important step in fabricating solar cells using the alloys. Several effects of the $CdCl_2$ treatment are believed to enhance the conversion performance of the alloy films, including increasing the grain size, improving the alloy/CdS interface, and reducing the lattice mismatch there. For evaluation purposes, the $CdCl_2$ treatment was performed on a 2 cm × 3 cm piece of each sample placed in a one inch diameter quartz tube. The source was made by evaporating a methanol solution of the chloride on a warm glass plate. The sample was placed on the source plate with the film side face down and a 1 mm gap between the film surface and the source plate. A typical 30 minute $CdCl_2$ treatment was performed on the $Cd_{1-x}Mg_xTe$ films at a temperature of 387°C. To treat the $Cd_{1-x}Mn_xTe$ films, there were two post-deposition approaches. In one case, the $CdCl_2$ vapor treatment was carried out on the films under the same conditions as for $Cd_{1-x}Mg_xTe$, and in the

other, a two-step process was applied in which a high temperature annealing step was carried out at a temperature of 520°C for 10 minutes under 2% H_2/Ar, followed by a standard $CdCl_2$ vapor treatment at 385°C for 30 minutes in dry air.

In order to compare the optical results before and after $CdCl_2$ treatment, over 1 μm thickness pure CdTe films were magnetron sputtered onto soda-lime glass at 250°C. For these CdTe films, a $CdCl_2$ treatment in dry air ambient was performed at a temperature of 387°C with different times optimized for the film thicknesses.

6.1.2.2 Data analysis and results

A rotating compensator multichannel spectroscopic ellipsometer with a 0.75 - 6.5 eV photon energy range was used to investigate the optical properties of the as-deposited and annealed films. The information extracted from SE measurements is very useful for assessing the surface and bulk quality of samples.

As-deposited $Cd_{1-x}Mg_xTe$ and $Cd_{1-x}Mn_xTe$ optical properties
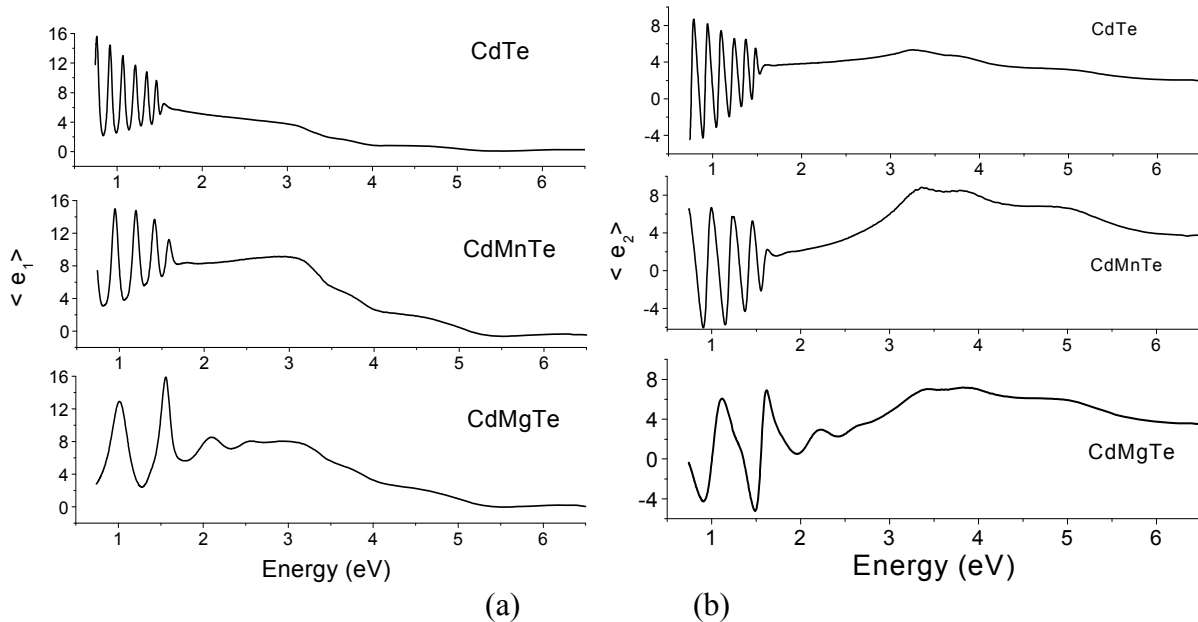
Figure 6.2. Real (a) and imaginary (b) parts of pseudo-dielectric function of RF sputtered CdTe ($E_g = 1.50$ eV), $Cd_{1-x}Mn_xTe$ ($E_g = 1.63$ eV) and $Cd_{1-x}Mg_xTe$ ($E_g = 1.61$ eV) films.

Figure 6.2 shows the pseudo-dielectric functions of RF magnetron sputtered CdTe, $Cd_{1-x}Mn_xTe$, and $Cd_{1-x}Mg_xTe$ films. The thickness of CdTe, $Cd_{1-x}Mn_xTe$ and $Cd_{1-x}Mg_xTe$ films are 1.41 μm, 1.0 μm and 0.18 μm, respectively. The band gaps of 1.63 eV for the $Cd_{1-x}Mn_xTe$ film and 1.61 eV for the $Cd_{1-x}Mg_xTe$ film were estimated from optical transmission measurements. These two alloy films as well as the CdTe film are transparent below their band gaps, and the spectral density of interference fringes in the lower energy range scales with the film thickness. In the high energy range from 2.0 eV to 6.5 eV, features are observed corresponding to the higher energy band gaps at the critical points in the joint density of states. The imaginary part of the pseudo-dielectric function is most closely related to the joint density of

states and thus the absorptive behavior of films; however, both real and imaginary parts provide sensitivity to the film crystalline quality and surface structure. In fact, the broadening energies of the peaks at the CPs decrease with an increase in crystalline grain size arising from the polycrystalline structure. The band structure critical point parameters including the energy gap and broadening energy can be deduced from $\varepsilon(E)$ by fitting to a standard analytic line shape [6]

$$\varepsilon(E) = Ae^{i\phi}\Gamma^{\mu}/[(2E - 2E_j + i\Gamma)^{\mu}], \qquad (1)$$

where A is the CP amplitude, Γ and ϕ are the broadening energy and phase angle, and E_j and μ are the threshold energy and exponent, the latter defined by the nature of the singularity in the electronic joint density of states. These parameters are readily determined by fitting second-derivative spectra $d^2\varepsilon(E)/dE^2$. For the ternary alloy system, once relationships have been established between the composition and the critical point (CP) energies in the band structure, as determined from the dielectric function $\varepsilon(E)$, such relationships can be used to estimate the composition of any unknown alloy [6,7]. Figure 6.3 shows the experimental second-derivative spectra in the pseudo-dielectric function $<\varepsilon(E)>$ of an as-deposited $Cd_{1-x}Mn_xTe$ sample, along with best fit results obtained using Eq. (1).
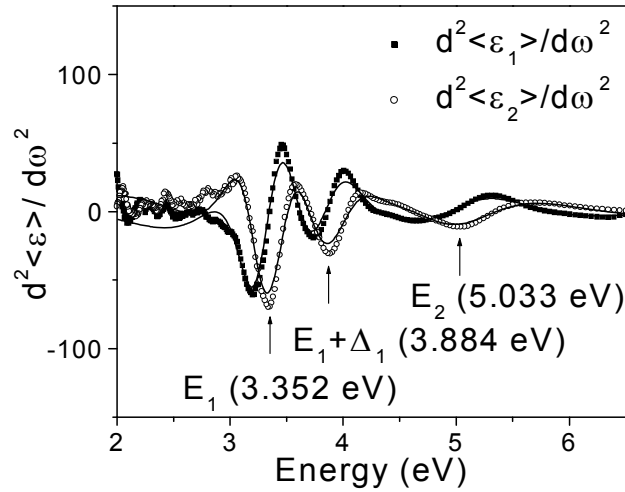
Figure 6.3. Best fit to the second derivative of the pseudo-dielectric function for an as-deposited $Cd_{1-x}Mn_xTe$ film (lines); the circles represent experimental data. The three CP transitions, E_1, $E_1 + \Delta_1$, and E_2, are indicated by arrows with energies of 3.352, 3.884, and 5.033 eV, respectively. The composition of x=0.06 can be estimated by the empirical relationship between E_1 and the composition [8].

A comparison of pseudo-dielectric functions of a $Cd_{0.94}Mn_{0.06}Te$ film after Br_2/methanol etch and after selected times of long term storage is given in Figure 6.4, whereas the corresponding results over the period of an hour after the Br_2/methanol etch step are given in Figure 6.5. The freshly-deposited sample exhibits higher amplitudes in $<\varepsilon>$ than a sample that has been stored. The data for the $Cd_{0.94}Mn_{0.06}Te$ sample in Figure 6.2 were taken one week after film deposition. Thus, it is reasonable to interpret the relatively low amplitudes to surface oxidation. By tracking $<\varepsilon_2>$ values during Br_2/methanol chemical etching processes, one can
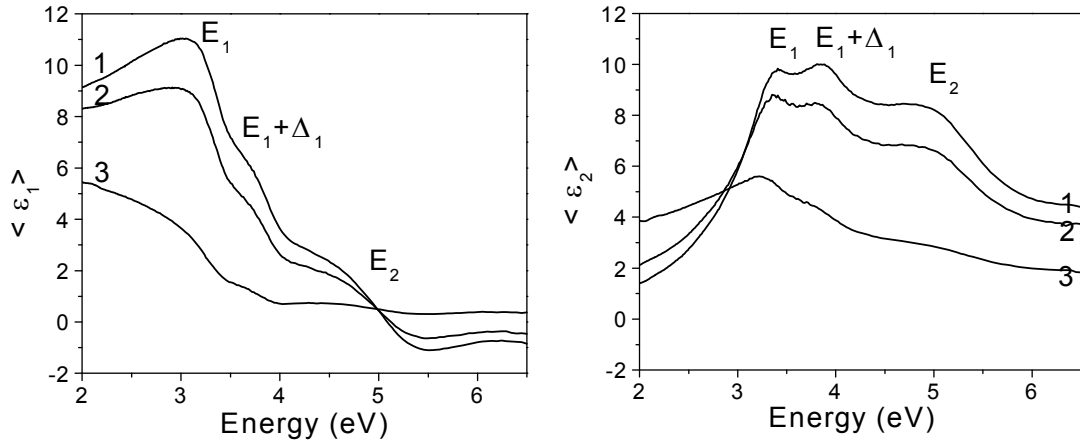
Figure 6.4. Pseudo-dielectric function of $Cd_{0.94}Mn_{0.06}Te$ samples after different storage times in laboratory ambient: (1) immediately after Br_2/methanol etch; (2) 3 weeks after deposition; and (3) 1.5 years after deposition.
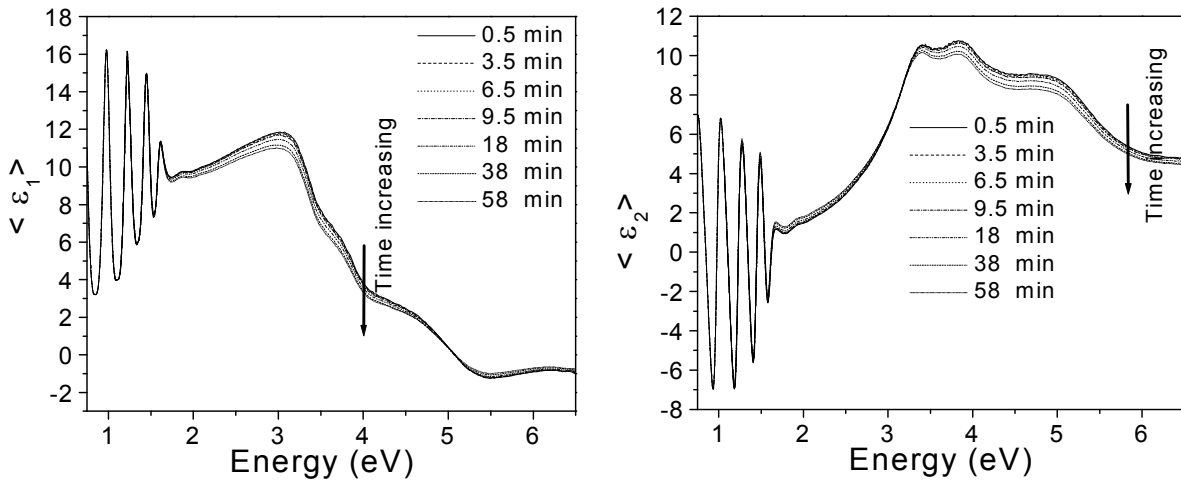
Figure 6.5. Variation of the pseudo-dielectric function of $Cd_{0.94}Mn_{0.06}Te$ with time after Br_2/methanol etching, measured *in situ* during exposure to laboratory ambient.
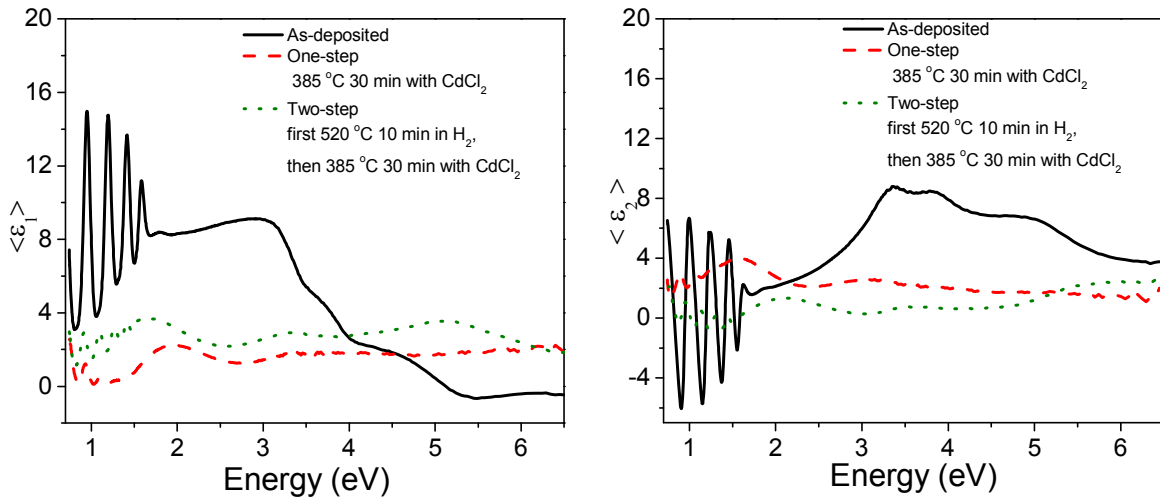
Figure 6.6. Pseudo-dielectric functions of as-deposited and treated $Cd_{0.94}Mn_{0.06}Te$ samples.

30

develop an optimum procedure to remove the oxide, and achieve the most abrupt interface to the ambient. For the results in Figure 6.4, the E_1, $E_1 + \Delta_1$, and E_2 critical-point structures can be seen clearly in all spectra. The sample measured immediately after etching by Br_2/methanol chemical solution showed the highest amplitudes of the pseudo-dielectric function in the higher energy region. In fact, the maximum values in Figure 6.4 are in accord with those of epitaxial films [8] and bulk crystals [9]. Thus, the pseudo-dielectric function after etching is expected to be very close to true dielectric function with only small deviations due to residual surface roughness or a Te-rich layer generated by the etching process.

Continuous changes in the pseudo-dielectric function induced by sample exposure to laboratory ambient can be observed in real time by SE. Figure 6.5 shows the variation of the pseudo-dielectric function of the 3-week-old $Cd_{0.94}Mn_{0.06}Te$ sample exposed to air after Br_2/methanol etching. For such measurements, the native oxide layer was removed by 0.01-0.02% Br_2/methanol in a few seconds of etching time. Upon exposure of the clean sample to air, the pseudo-dielectric function does not change significantly during the initial several minutes; however, with increasing time on a longer scale, both real and imaginary parts of the pseudo-dielectric function gradually decrease. In fact, the imaginary part of the pseudo-dielectric function near the $E_1 + \Delta_1$ CP energy (~ 3.88 eV) decreased by 5% in one hour.

Optical properties of $CdCl_2$-treated and $Cd_{1-x}Mn_xTe$ and $Cd_{1-x}Mg_xTe$

Figure 6.6 shows the pseudo-dielectric function of as-deposited (3-week-old) and annealed $Cd_{0.94}Mn_{0.06}Te$ samples. Using the dielectric function obtained from the Br_2/methanol-etched $Cd_{0.94}Mn_{0.06}Te$ sample and assuming Te oxide (TeO_2) on the surface, a simple 3-layer model of oxide/$Cd_{0.94}Mn_{0.06}Te$/glass could be employed to fit the experimental results for the as-deposited sample, and the thickness of TeO_2 layer was found to be ~ 35 Å. For the annealed sample, however, it was difficult to fit the experimental data due to lack of reference dielectric functions for the surface layer components. In particular, for the sample that was vapor treated with $CdCl_2$ at 385°C, the pseudo-dielectric function was much different from that of the as-deposited samples. It was further observed that even after the treated films were etched using several etching steps of 0.04 volume % Br_2 in methanol, the pseudo-dielectric function shape showed much different spectral behavior from the as-deposited sample. This suggests that the top layer is substantially modified during treatment, both chemically and morphologically.
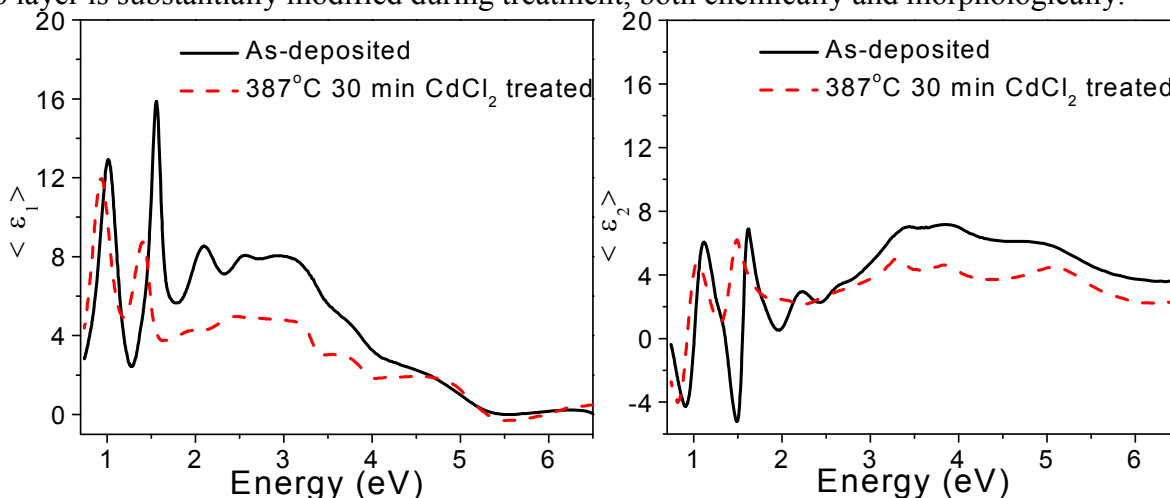

Figure 6.7. Pseudo-dielectric functions of as-deposited and annealed $Cd_{1-x}Mg_xTe$ samples.

Figure 6.7 shows the pseudo-dielectric function of as-deposited and CdCl$_2$-treated Cd$_{1-x}$Mg$_x$Te samples. For the CdCl$_2$-treated Cd$_{1-x}$Mg$_x$Te sample, much less deterioration in the bulk optical characteristics is observed compared with Cd$_{1-x}$Mn$_x$Te, suggesting that the CdCl$_2$ treatment may be effective for Cd$_{1-x}$Mg$_x$Te PV devices. Dielectric functions of as-deposited and CdCl$_2$ treated samples over the energy range of 3.0 ~ 6.0 eV are shown in Figure 6.8. For these measurements, the films were previously etched using many steps, each consisting of brief immersion in a 0.04 volume % Br$_2$ in methanol solution. The original intent of this process was to remove oxides that develop on as-deposited and CdCl$_2$-treated CdTe films due to their exposure to the laboratory and treatment ambients. Interestingly, it has been found that successive etching steps lead to a significant step-wise smoothening of the film surface simultaneously with decreasing bulk layer thickness due to step-wise film dissolution. In fact, a roughness layer of thickness of up to a micron or more can be eliminated in several successive etching steps, and ultimate stabilization of the roughness thickness at ~20-40 Å can be observed. It is under stable, smooth-surface conditions that the measurements of Figure 6.8 are made. Under these conditions, the dielectric function deduced from the measured ellipsometry spectra is reasonably representative of the true dielectric function, enabling determination of the critical point energies and widths by dielectric function fitting. It is known that the etching treatments lead to a Te-rich surface layer (~10 Å); however, its effect is expected to be smaller than that of the residual roughness and has been neglected in this study.

Figure 6.8(a) compares the dielectric function of Br$_2$/methanol-etched Cd$_{1-x}$Mg$_x$Te in the as-deposited (left) and CdCl$_2$-treated (right) states. The results may differ somewhat from the true dielectric function due to the presence of the residual roughness and a Te-rich surface layer. This Cd$_{1-x}$Mg$_x$Te film was sputter-deposited to a thickness of 0.18 μm on a soda-lime glass slide. The key observation in the comparison of the panels of Figure 6.8(a) is that the critical points E$_1$, E$_1$+Δ_1, and E$_2$ are observed at similar energy positions in both sample states (any observed shifts being due to incomplete accounting of surface effects), and in fact become sharper upon CdCl$_2$ treatment. This is an indication that the composition of the film is retained upon treatment and that the crystalline grain size increases, as well. For comparison, Figure 6.8(b) shows the corresponding results for CdTe (i.e., with no alloying), in which case similar behavior is observed. In contrast, for Cd$_{1-x}$Mn$_x$Te in Figure 6.8(c), the CdCl$_2$ treatment leads to a complete loss of the critical point structures and these cannot be recovered by continued etching. This demonstrates that the treatment leads to a significant chemical modification of the Cd$_{1-x}$Mn$_x$Te film that can account for its poor performance when incorporated into actual devices. The fact that the Cd$_{1-x}$Mg$_x$Te does not experience such a modification upon CdCl$_2$ treatment and retains the band structure characteristics of the as-deposited film (along with a significant increase in grain size) demonstrated promise for the development of devices from this material.

Quantitative information can be obtained from fits to the pseudo-dielectric functions of Figure 6.8 which provide the energy positions and widths of the dielectric function peaks. These results are given in Figure 6.8 as the solid lines for all films except for the CdCl$_2$-treated Cd$_{1-x}$Mn$_x$Te in which case the critical point structure is lost. The critical point parameters including the energy positions E_j and widths Γ_j are presented in Table 6.1. Among the key observations of Table 6.1 include:

(i) retention of the critical point structure for Cd$_{1-x}$Mg$_x$Te upon CdCl$_2$ treatment without a significant change in the energy positions (in consideration of surface variations), indicating success of alloying in the CdCl$_2$-treated films;

(ii) reduction of the critical point transition widths upon CdCl$_2$ treatment for the CdTe

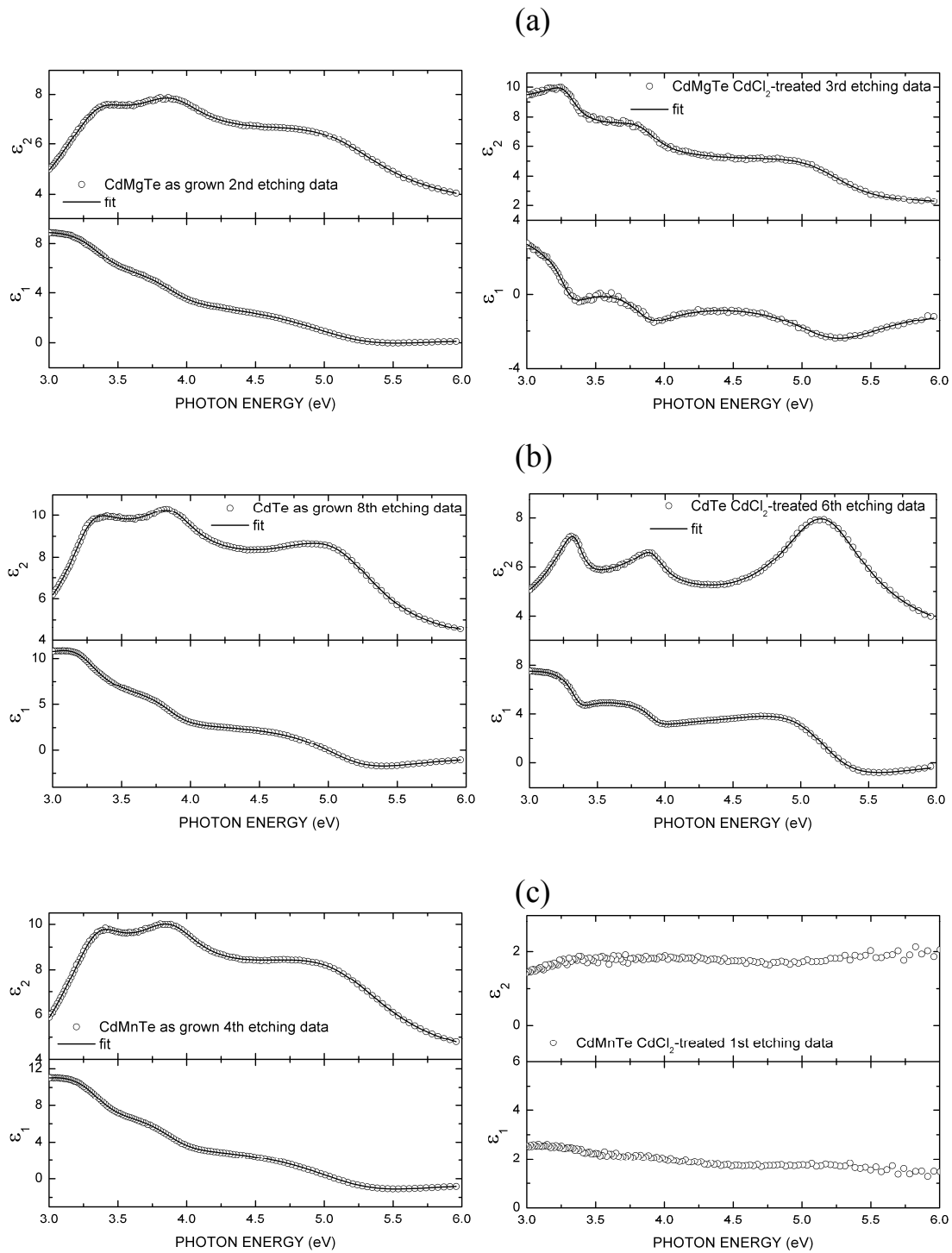Figure 6.8 Pseudo-dielectric functions, i.e., optical properties deduced without complete correction of surface effects, for as-deposited and $CdCl_2$-treated films as obtained by SE after Br_2/methanol etching to improve the surface quality (points); (a) $Cd_{1-x}Mg_xTe$; (b) CdTe; (c) $Cd_{1-x}Mn_xTe$; the solid lines show the results of fits to extract critical point energies and widths.

and $Cd_{1-x}Mg_xTe$, an indication of an increase in grain size or a reduction in defect density;

(iii) increase of the critical point transition widths for the as-deposited alloys compared with the as-deposited CdTe, possibly due to a smaller grain size in the as-deposited alloy films; and

(iv) similar critical point widths for the $CdCl_2$-treated CdTe and $Cd_{1-x}Mg_xTe$, indicating the effectiveness of the treatment in improving the alloy.

Table 6.1. Parameters obtained in the fits to the dielectric functions of Figure 6.8.

	CdTe as-dep.	CdTe $CdCl_2$-treat.	$Cd_{1-x}Mg_xTe$ as-dep.	$Cd_{1-x}Mg_xTe$ $CdCl_2$-treat.	$Cd_{1-x}Mn_xTe$ as-dep.	$Cd_{1-x}Mn_xTe$ $CdCl_2$-treat.
E_0 (eV)	1.497	1.499	1.615	1.633	1.548	---
E_1 (eV)	3.274	3.331	3.354	3.303	3.363	---
$\Gamma(E_1)$ (eV)	0.411	0.200	0.480	0.216	0.430	---
$E_1+\Delta_1$ (eV)	3.844	3.883	3.901	3.878	3.914	---
$\Gamma(E_1+\Delta_1)$ (eV)	0.484	0.368	0.520	0.309	0.483	---
E_2 (eV)	5.193	5.208	5.179	5.197	5.182	---
$\Gamma(E_2)$ (eV)	0.993	0.796	1.252	0.879	1.215	---

Furthermore, two additional $Cd_{1-x}Mg_xTe$ samples prepared by magnetron sputtering from alloy targets were studied in detail by ex situ SE. The goal of this study was to compare films prepared with low Mg content and band gaps in the range E_g = 1.60 - 1.65 eV with those prepared at much higher Mg content. This comparison was performed on as-deposited films without $CdCl_2$ treatment.

- For the comparison sample (CGT42), the target was CdTe (80 wt.%) + MgTe (20 wt.%), and $Cd_{1-x}Mg_xTe$ deposition was performed on a soda lime glass substrate at a temperature of 200°C using 50 W RF power at the target, 20 mTorr Ar pressure, and 30 sccm Ar flow. The deposition time was 2 hours, and the $Cd_{1-x}Mg_xTe$ film thickness was ~ 0.3 μm.
- For the higher Mg content sample (CGT92), the target was CdTe (60 wt.%) + MgTe (40 wt.%), and $Cd_{1-x}Mg_xTe$ deposition was performed on an aluminosilicate glass substrate at a temperature of 290°C using 50 W RF power at the target, 5 mTorr Ar pressure, and 30 sccm Ar flow. The deposition time was 6 hours, and the $Cd_{1-x}Mg_xTe$ film thickness was ~ 2.9 μm.

The spectroscopic ellipsometry was performed on these two samples at angles of incidence of 60° and 65°, respectively. The photon energy range of the instrument is 0.74~6.50 eV. A two-layer surface-roughness/bulk model for the film was used to analyze the experimental data (ψ, Δ). The dielectric function of the bulk layer was modeled on the basis of the analytical formula

$$\varepsilon = \Sigma_j \, [A_j \exp(i\phi_j)] * [\Gamma_j/(2E_j - 2E - i\Gamma_j)]^{\mu_j},$$

where the oscillators labeled j = 1, 2, 3, 4,

correspond to the E_0 (band gap), E_1, $E_1+\Delta_1$, and E_2 critical point transitions and $j=5$ corresponds to a broad background oscillator. Each oscillator has five free parameters: amplitude A_j, energy E_j, width Γ_j, phase ϕ_j, and exponent μ_j. In this analysis, the focus is on the critical point energies E_j and the width Γ_0 of the lowest band gap critical point.

Figure 6.9. Pseudo-dielectric function obtained directly from experimental (ψ, Δ) data using a single interface conversion formula for a $Cd_{1-x}Mg_xTe$ sample prepared from a target of CdTe (80 wt.%) + MgTe (20 wt.%) (CGT42). The straight line describes experimental data and the dashed line describes the best fit result.
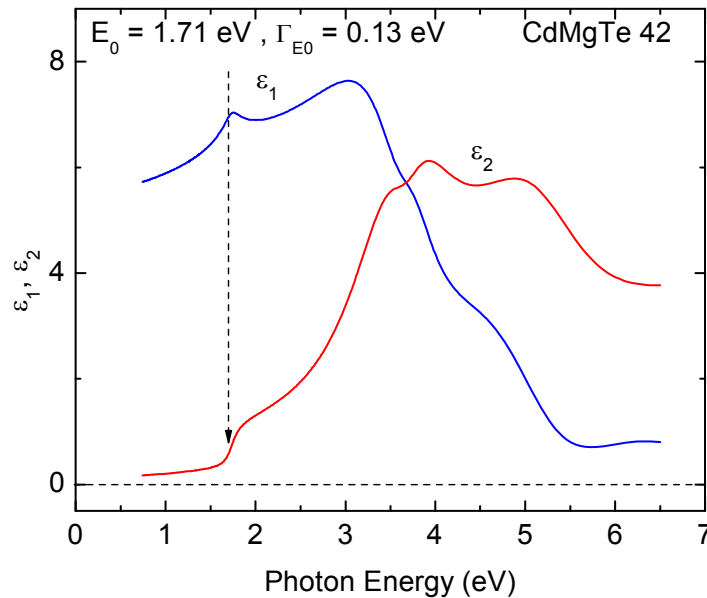
Figure 6.10. Best fit analytical dielectric function obtained from an analysis of the experimental (ψ, Δ) data for a $Cd_{1-x}Mg_xTe$ sample prepared from a target of CdTe (80 wt.%) + MgTe (20 wt.%) (CGT42).

The energies provide information on the band gaps, alloying, and strain, and the width of the E_0 critical point provides information on defects, grain size, and disorder. Figure 6.9 shows the pseudo-dielectric function data for the lower Mg content $Cd_{1-x}Mg_xTe$ sample (CGT42) and the best fit to these data. Figure 6.10 shows the true dielectric function of this $Cd_{1-x}Mg_xTe$ film which is extracted in the best fit. The deduced band gap, 1.71 eV, is wider than that of the previous sample due to the preparation procedure, and the broadening parameter is 0.13 eV. This band gap corresponds to a composition of $x = 0.15$ using the relationship established previously. Optical transmission spectroscopy yielded a band gap value in agreement with the SE result.

Figures 6.11 and 6.12 show the results for the higher Mg content sample (CGT92). The band gap of this film is 1.98 eV, and the broadening parameter is 0.16 eV. The band gap corresponds to a composition of $x = 0.30$, indicating a linear relationship between film and target composition for the two samples.
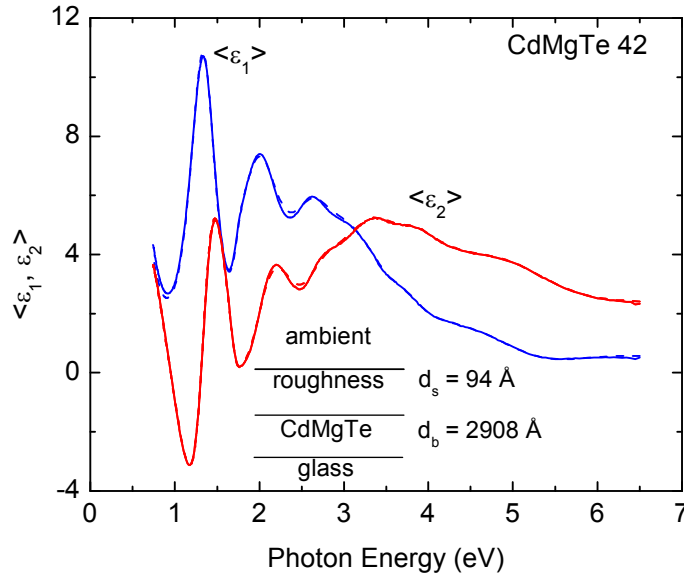

Figure 6.11. Pseudo-dielectric function obtained directly from experimental (ψ, Δ) data using a single interface conversion formula for a $Cd_{1-x}Mg_xTe$ sample prepared from a target of CdTe (60 wt.%) + MgTe (40 wt.%) (CGT92). The straight line describes experimental data and the dashed line describes the best fit result.
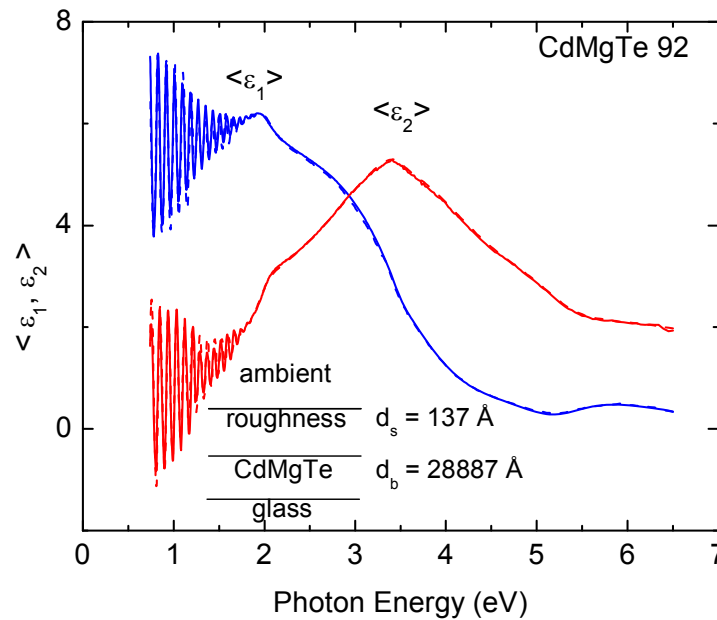
Table 6.2 shows the values of the fundamental gap energy E_0 and its width, as well as the energies of the higher energy critical points E_1, $E_1+\Delta_1$, E_2, for the two $Cd_{1-x}Mg_xTe$ samples. Also shown for comparison are the corresponding results for pure CdTe before and after the $CdCl_2$ treatment. (Note that the shifts in the energies of critical points upon $CdCl_2$ treatment for CdTe are due to relaxation of strain and the narrowing of the E_0 peak is due to an increase in grain size.) It is clear that the E_0 band gap increases as the target alloy composition increases; the use of 20 wt.% MgTe in the target does not lead to significant broadening of the E_0 transition relative to pure untreated CdTe. However, 40 wt.% MgTe leads to a significant broadening effect as a result of either a smaller grain size or increased disorder in the film due to alloying. The non-monotonic behavior observed in the E_1 and $E_1+\Delta_1$ higher energy gaps with alloying are likely to be due to changes in electronic structure as well as strain in the films.
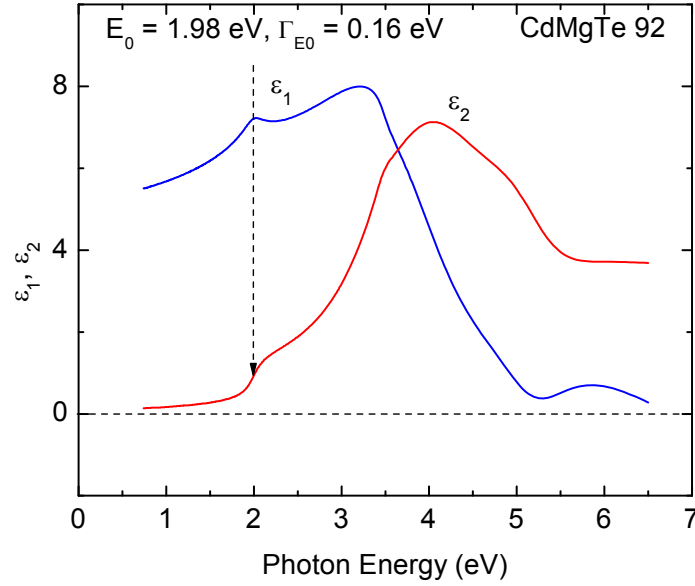
Figure 6.12 Best fit analytical dielectric function obtained from an analysis of the experimental (ψ, Δ) data for a $Cd_{1-x}Mg_xTe$ sample prepared from a target of CdTe (60 wt.%) + MgTe (40 wt.%) (CGT92).

Table 6.2. Critical point energies and E_0 gap broadening for two $Cd_{1-x}Mg_xTe$ alloys from spectroscopic ellipsometry.

	CdTe CdCl$_2$-treat.	CdTe untreated	$Cd_{1-x}Mg_xTe$ 42 (20 wt.% MgTe)	$Cd_{1-x}Mg_xTe$ 92 (40 wt.% MgTe)
E_0 (eV)	1.476	1.529	1.710	1.983
$\Gamma(E_0)$ (eV)	0.045	0.130	0.128	0.161
E_1 (eV)	3.309	3.195	3.567	3.479
$E_1+\Delta_1$ (eV)	3.888	4.025	3.725	3.816
E_2 (eV)	5.163	5.260	5.175	5.143

6.1.3 Bottom cell material: $Hg_xCd_{1-x}Te$

6.1.3.1 $Hg_xCd_{1-x}Te$ films preparation

Efforts have also focused on the optical characterization of as-deposited $Hg_xCd_{1-x}Te$ films grown at different substrate temperatures for use as a bottom cell absorber material. The $Hg_xCd_{1-x}Te$ films were deposited by rf magnetron sputtering on 1 mm thick soda-lime glass, using a sputtering target containing 40 weight % of Hg, i.e. HgTe (40 wt.%) + CdTe (60 wt.%). Films were grown at different temperatures, including 23°C, 44°C, 70°C, 85°C, 97°C, and 153°C. Optical characterization was performed in order to determine the variation of band gap with substrate temperature. In addition, $CdCl_2$ post-deposition treatments were performed on the $Hg_xCd_{1-x}Te$ films. The deposition temperature of interest is on the order of 100°C. The higher temperature of the post-deposition process has been shown in CdTe to increase the grain size and thus improve the efficiency of the cells. Two stages were explored; an anneal was carried out in

an inert gas at 387°C and then a $CdCl_2$ vapor treatment at the same temperature. Ex situ spectroscopic ellipsometry data were acquired on as-deposited and $CdCl_2$-treated $Hg_xCd_{1-x}Te$ films before and after Br_2/methanol etching.

6.1.3.2 Data analysis and results

Figure 6.13 shows the band gap of $Hg_xCd_{1-x}Te$ films in the as-deposited state for different substrate temperatures, while Figure 6.14 shows the dielectric functions from the inversion process and from the corresponding analytical model fit. All films were deposited at an Ar pressure of 10 mTorr and an RF power of 27 W.
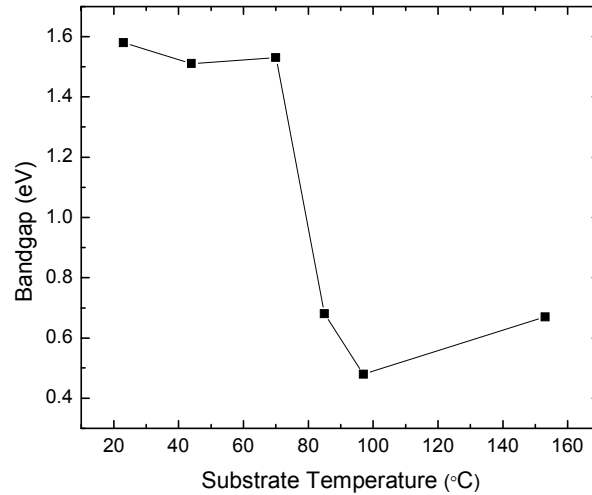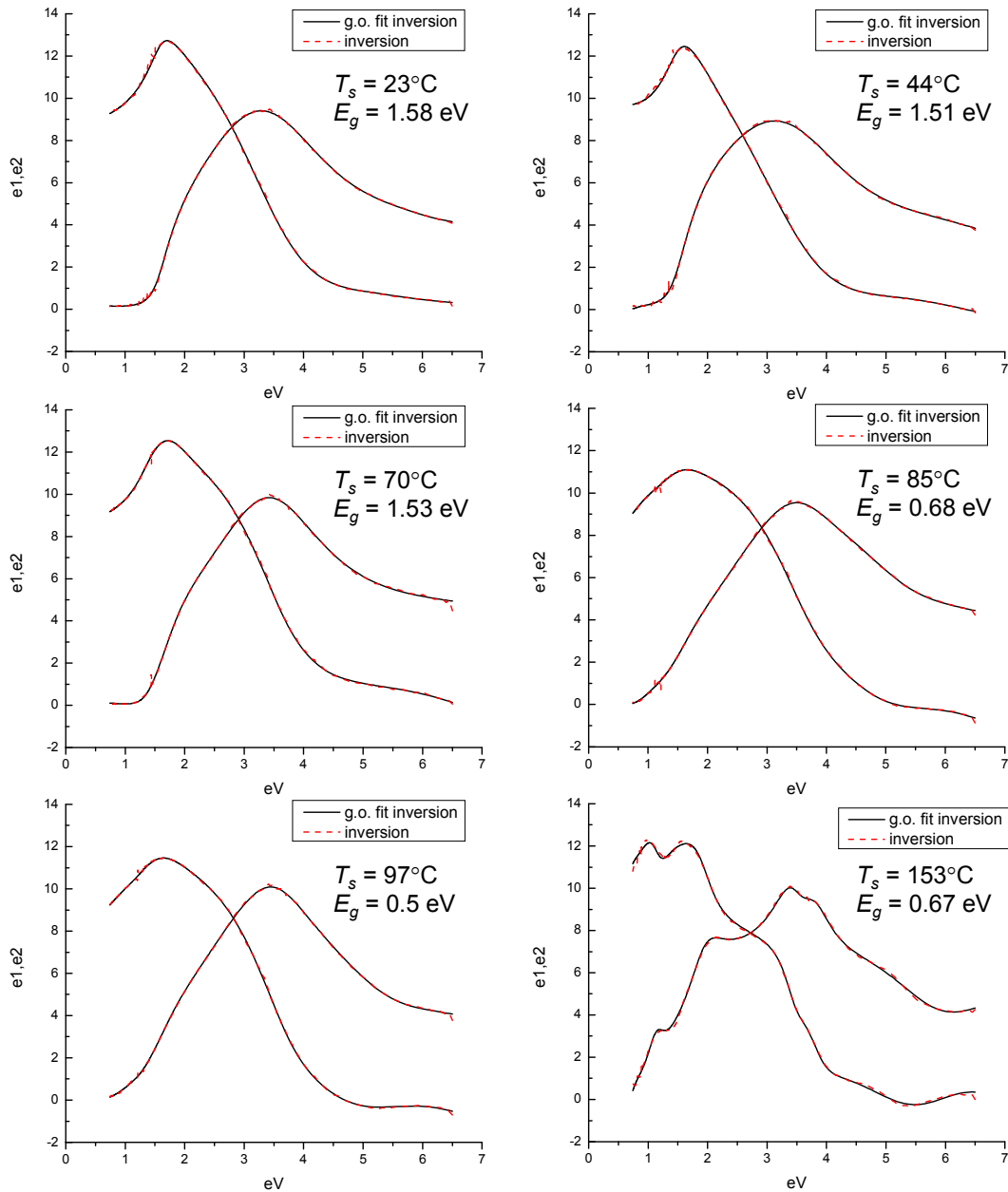

Figure 6.13. Band gaps of as-deposited Hg_xCd_{1-x} Te films with substrate temperatures from 23°C to 155°C; the deposition pressure was 10 mTorr and the RF power was 27 W.

Figures 6.13 and 6.14 show the band gaps and dielectric functions for the $Hg_xCd_{1-x}Te$ alloy films prepared as a function of temperature. For the dielectric function, results are presented that have been obtained both by inversion of the (ψ, Δ) data and by fitting assuming an analytical model. The agreement between the two methods supports the validity of the functional form of the analytical model. Figure 6.13 shows that the band gap decreases abruptly at a substrate temperature of about 75°C. At low temperatures the deposited films are consistent with nanocrystalline CdTe of band gap of ~1.5 eV. It is possible that nanoscale Hg inclusions exist, giving rise to a broad plasmon resonance. The semiconductor component of the films grown at lower temperatures, i.e. at room temperature, 44°C, 70°C, 87°C and 97°C, must have large number of grain boundaries leading to extremely small grain size in accordance with the wide broadening values, and hence nearly amorphous films. In the film prepared at the highest temperature of 153°C, semiconducting $Hg_xCd_{1-x}Te$ with x~0.4 appears to have been obtained with a larger grain size. These trends are confirmed by XRD measurements and films grown at 85°C and 97°C appear to have small grains coalesced to form larger grains with diffused grain boundaries.

Figures. 6.14 Dielectric functions from the inversion process and from the corresponding analytical
model fit for as-deposited $Hg_xCd_{1-x}Te$ films prepared with different substrate temperatures.

Figure 6.15 presents a comparison of the pseudo-dielectric functions of as-deposited and
$CdCl_2$ treated $Hg_xCd_{1-x}Te$ films, including the results without and with an etching step. The key
observations of Figure 6.15 shows include (i) the blue shift of the critical energy point positons
for $Hg_xCd_{1-x}Te$ upon $CdCl_2$ treatment, indicating the loss of Hg content in the alloy film after the
treatment; (ii) reduction of the critical point transition widths upon $CdCl_2$ treatment for the
$Hg_xCd_{1-x}Te$, an indication of an increase in grain size or a reduction in defect density. This post-
deposition treatment has proved to be the most challenging aspect of $Hg_xCd_{1-x}Te$ and other alloy

film preparation and further work is needed to optimize these processes specifically for the alloys.
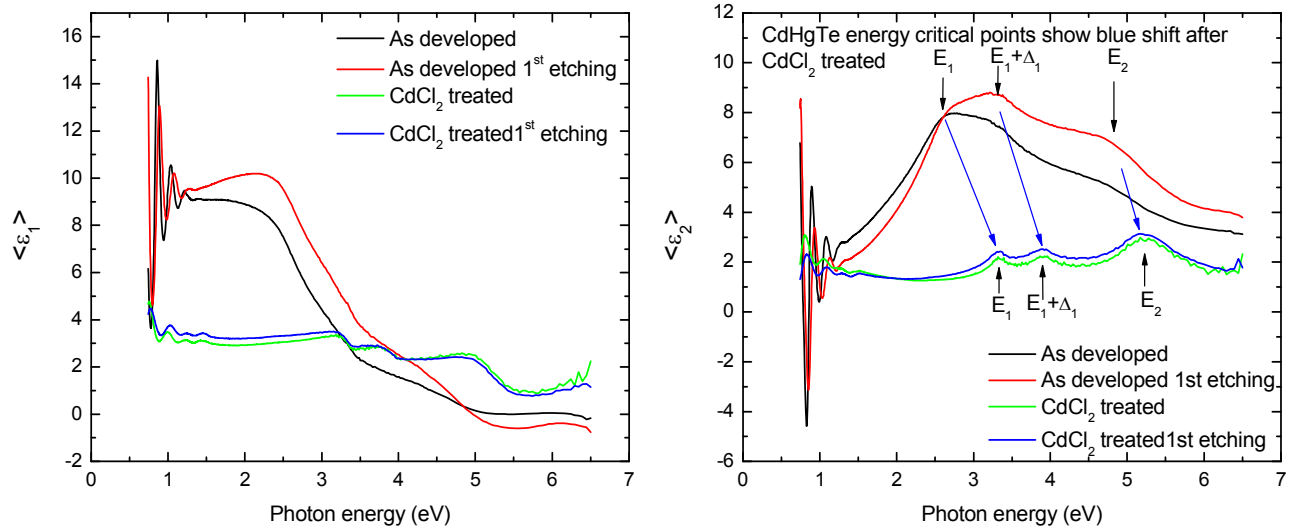

Figure 6.15. Comparison of the pseudo-dielectric function of as-deposited and $CdCl_2$ treated $Hg_{1-x}Cd_xTe$ films, including results before and after a Br_2/methanol etching step.

7. Studies with collaborators

7.1 X-ray photoelectron spectroscopy of CdMgTe (Heske/Weinhardt, University of Nevada Las Vegas)

During Phase III we collaborated with the group of Prof. Clemens Heske of UNLV for XPS studies of polycrystalline films prepared following the procedures used for cell fabrication. Thus we prepared a series of thin films to study the window / main junction interfaces. This involved standard alkaline soap cleaning of the Pilkington Tec-15 substrates on 3 mm soda-lime glass. Magnetron sputter deposition of the CdS layer on Tec-15 was carried out following standard procedures in a turbo-pumped stainless steel cross chamber with tantalum wire radiative heating of the Tec-15. The chamber base pressure was 5×10^{-7} Torr and 2×10^{-6} Torr during substrate heating. The sample was then transferred in air to the adjacent cryo-pumped deposition chamber with tungsten-halogen lamp substrate heating for the sputter deposition of CdMgTe. The base pressure of the second deposition chamber was 1.2×10^{-7} T and 8×10^{-7} T during lamp heating of the substrate. Sputter deposition was carried out in Ar of 5N purity for both the CdS and CdMgTe. The samples used in this study were:

- cleaned Tec-15
- Tec-15/CdS (130 nm)
- Tec-15/CdS/CdMgTe (1 nm)
- Tec-15/CdS/CdMgTe (3 nm)
- Tec-15/CdS/CdMgTe (5 nm), and
- Tec-15/CdS/CdMgTe (50 nm).

The objective of this study was to obtain information on band lineups for the system CdS/CdMgTe. Unfortunately, no reliable information could be obtained because of contamination from unexpected elements in the spectra.
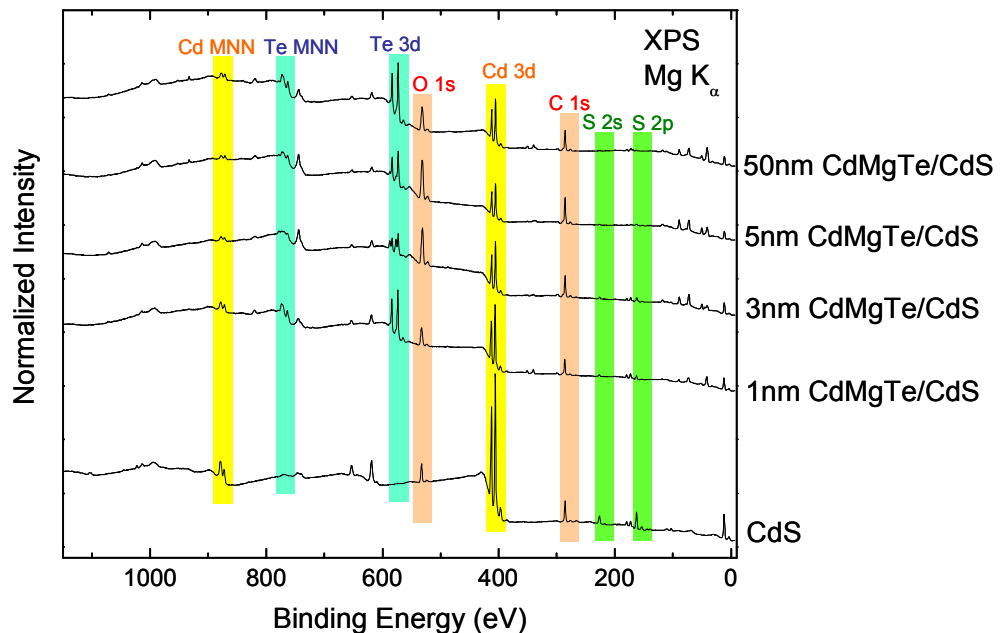

Figure 7.1 XPS spectra of sputtered thin films on commercial tin-oxide coated soda-lime glass. The CdS thickness was 130 nm in all cases.
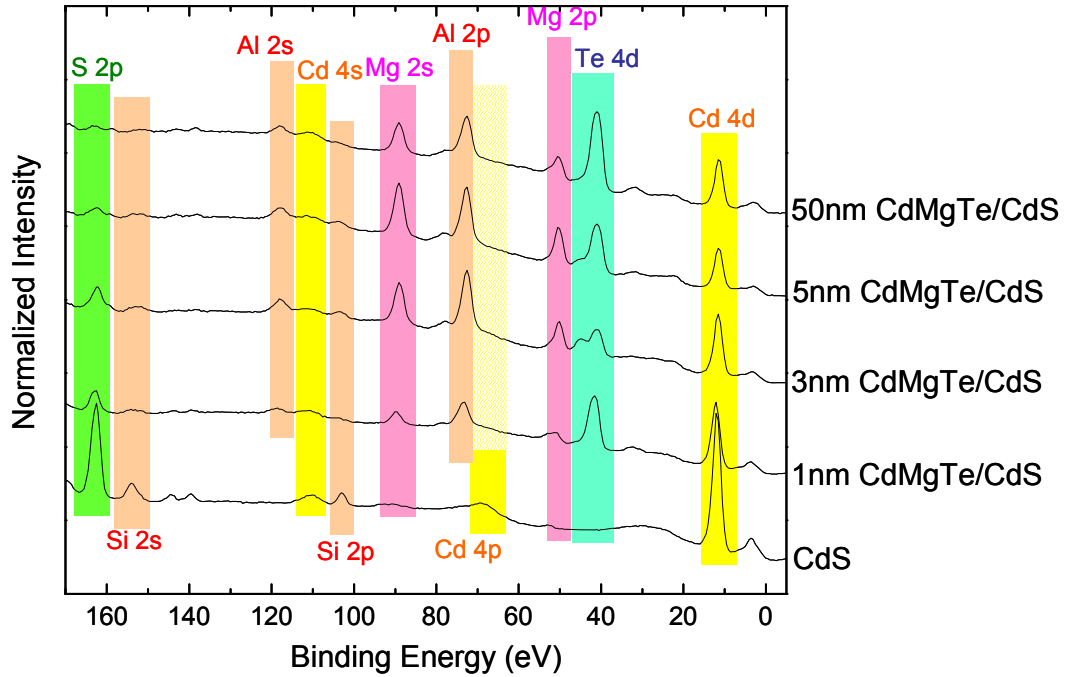
Figure 7.2 Low binding energy region of XPS spectra of Figure 7.1.

7.2 Thin CdTe as a top cell (filter) over a Si wafer (Rohatgi/Yelundur, Georgia Tech)

Although not a polycrystalline thin film material, crystalline or multicrystalline Si has an appropriate band gap for a bottom cell in a two-junction tandem. In order to explore the suitability of thin CdTe as a top cell with Si as a bottom cell, we supplied Vijay Yelundur with three plates having the following structure:

- Aluminum silicate glass (ASG) 1 mm thick
- ASG/ZnO:Al (~0.5 μm)
- ASG/ZnO:Al/CdS (0.13 μm) / CdTe (1.0μm).

The last plate was a complete solar cell except for the back contact. With carefully chosen thicknesses for a back contact of (e.g.) ZnTe:N/ITO, it is possible to increase the optical transmission of the structure by reducing the reflection at the CdTe/air interface. This reflective loss is about 30%. Nevertheless, the use of these structures as filters above the Si wafer provides a insight into some of the practical issues that might arise especially with a four-terminal tandem device.

Table 7.1   Si cell response uncovered and with three different filters structures.

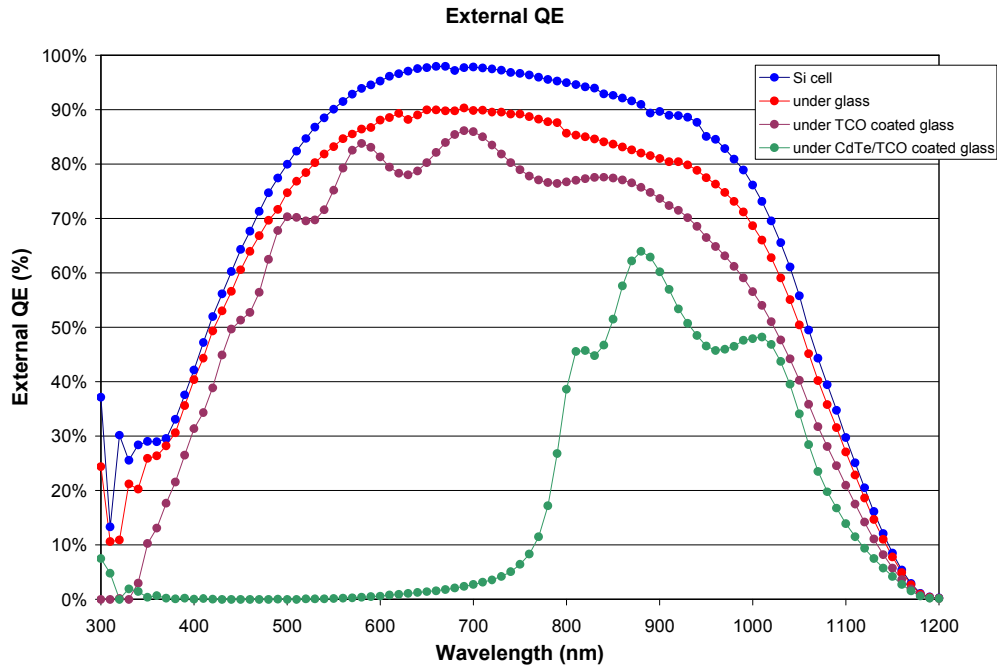|	Area (cm^2)	V_{oc} (V)	I_{sc} (A)	J_{sc} (mA/cm^2)	FF (%)	Eff (%)
b3-4	4	0.6278	0.137	34.3	78.6	16.9
b3-4glass	4	0.6253	0.128	31.9	78.7	15.7
b3-4TCO	4	0.6228	0.117	29.2	78.7	14.3
b3-4CdTe	4	0.5823	0.027	6.7	77.5	3.0

Figure 7.3 External spectral quantum efficiency for a Si cell unfiltered (blue), under 1mm ASG (red), ZnO:Al-coated ASG (purple), and CdTe/CdS/ZnO:Al/ASG (green).

References (from section 1 through 7)

1 J.M. Hartman, J. Cibert, F. Kany, H. Mariette, M. Charleux, P. Alleysson, R. Langer, G. Feuillet, *J. Appl. Phys.*, **80**(1996)6257-6265.

2 A. Gupta, V. Parikh, and A. D. Compaan, *Solar Energy Materials and Solar Cells*, **90**, 2263 (2006).

3 A. Gupta and A. D. Compaan, *Applied Physics Letters,* **85**, 684 (2004).

4   J. Chen, J. Li, D. Sainju, K.D. Wells, N.J. Podraza, and R.W. Collins, *Proc. 4th World Conference on Photovoltaic Energy Conversion*, (IEEE, Piscataway NJ, 2006), p. 475.

5 S. Marsillac, V.Y. Parikh, and A.D. Compaan, *Solar Energy Mater. Solar Cells* **91**, 1398 (2007).

6 D. E. Aspnes, *Handbook on Semiconductors*, *(North-Holland, Amsterdam),* **2**, 126 (1980).

7 O. Castaing, J. T. Benhlal, R. Granger, and R. Triboulet, *J. Cryst. Growth* **159**, 1112 (1996).

8   Y. H. Hwang et al., *Jpn. J. Appl. Phys*. **40**, 5247 (2001).

9   P. Lautenschlager, S. Logothetidis, L. Vina, and M. Cardona*, Phys. Rev. B* **32**, 3811 (1985).

8 Publications

8.1 Refereed papers published or in press

1. "Sputtered $Cd_{1-x}Zn_xTe$ Films for Top Junctions in Tandem Solar Cells" Sung Hyun Lee, Akhlesh Gupta, ShanLi Wang, Alvin D. Compaan and Brian E. McCandless, Solar Energy Materials and Solar Cells (in press)

2. "All sputtered 14% CdS/CdTe thin-film solar cell with ZnO:Al transparent conducting oxide," Akhlesh Gupta and Alvin D. Compaan, Applied Physics Letters, **85** (2004) 684.

3. "High efficiency, magnetron sputtered CdS/CdTe solar cells," A.D. Compaan, A. Gupta, S.H. Lee, S. Wang and J. Drayton, Solar Energy, **77** (2004) 815-822.

4. "14% sputtered thin-film solar cells based on CdTe," A.D. Compaan, A. Gupta, J. Drayton, S-H Lee, S. Wang, Physica Status Solidi (b), **241** (2004) 779-782.

5. "Polycrystalline sputtered Cd(Zn, Mn)Te films for top cells in PV tandem structures," Sung Hyun Lee, Akhlesh Gupta and Alvin D. Compaan, Physica Status Solidi (c), **1**(4) (2004) 1042-1046.

6. "RF sputtered HgCdTe films for tandem cell applications" S.L.Wang, S.H.Lee, A.Gupta, and A.D.Compaan, Physica Status Solidi (c), **1**(4) (2004) 1046-1049.

7. S.H. Lee, A. Gupta, SL Wang, A.D. Compaan, and B. McCandless, "Sputtered CdZnTe films for to junctions in tandem solar cells," *Solar Energy Materials and Solar Cells*, **86**, 551-563 (2005).

8. A. Gupta and A.D. Compaan, "High efficiency 1 micron thick sputtered CdTe solar cells," *Proc. 31st IEEE Photovoltaic Specialists Conference-2005*, 235-238, IEEE Piscataway, N.J. 2005.

9. V.Y. Parikh, J. Drayton, S.L. Wang, A. Gupta, and A.D. Compaan, "Polycrystalline thin-film tandem solar cells cascaded by ZnTe/ZnO interconnects," *Proc. 31st IEEE Photovoltaic Specialists Conference-2005*, 430-433, IEEE Piscataway, N.J. 2005.

10. S.L. Wang, J. Li, J. Chen, R.W. Collins, A.D. Compaan, "Spectroscopic ellipsometry and atomic force microscopy studies of RF sputtered CdMnTe films," *Proc. 31st IEEE Photovoltaic Specialists Conference-2005*, 480-483, IEEE Piscataway, N.J. 2005.

11. Alvin Compaan, "Photovoltaics: clean electricity for the 21st century," *APS News*, April 2005, p. 6. [available on line at http://www.aps.org/apsnews/0405/040514.cfm]

12. S. Wang, J. Chen, J. Li, A. Gupta, R.W. Collins, and A.D. Compaan, "Ellipsometry studies of $CdCl_2$ treated CdTe and related ternary alloy films for solar cell applications," Mater. Res. Soc. Symp. Proc. **865,** F5.29 (2005).

13. D. Shvydka, V. Parikh, V.G. Karpov, and A.D. Compaan, "Spatial and temporal variations in electronic transport through a CdTe-based Schottky barrier,"Mater. Res. Soc. Symp. Proc. **865,** F12.2 (2005).

14. A. Gupta and A.D. Compaan, "High efficiency, 0.8 micron CdS/CdTe solar cells," Mater. Res. Soc. Symp. Proc. 865, F14.33 (2005).

15. A.D. Compaan, Solar Energy Materials & Solar Cells, "Photovoltaics: clean power for the 21st century" (in press).

16. Akhlesh Gupta, Viral Parikh, Alvin D. Compaan, Solar Energy Materials & Solar Cells, "High efficiency ultra-thin sputtered CdTe solar cells" (in press) V. Parikh, A. Vasko, A.D. Compaan, and S.X. Marsillac, "Transparent Back Contacts in CdTe/CdS: Evaluation for Tandem Cells," Mater. Res. Soc. Symp. Proc. 1012, Y2.8 (2007).

17. Viral Y. Parikh, S. Marsillac, R.W. Collins, Jie Chen, A.D. Compaan, "Hg1-xCdxTe as the Bottom Cell Material in Tandem II-VI Solar Cells ," Mater. Res. Soc. Symp. Proc. 1012, Y12.37 (2007).

18. Xavier Mathew, A. Vasko, J. Drayton, and A. Compaan, "Development of a Wide Band Gap Cd1-xMgxTe Film for Applications in Tandem Devices," Mater. Res. Soc. Symp. Proc. 1012, Y2.5 (2007).

19. X. Mathew, J. Drayton, V. Parikh, and A.D. Compaan, "Sputtered Cd1-xMgxTe Films for Top Cells in Tandem Devices," 2006 IEEE 4th World Conference on Photovoltaic Energy Conversion-Proceedings (IEEE Piscataway, N.J. 2006) pp. 321-326.

20. V. Y. Parikh, J. Chen, S.X. Marsillac, and A.D. Compaan, "Transparent back contacts and interconnect junctions for CdTe top cells," 2006 IEEE 4th World Conference on Photovoltaic Energy Conversion-Proceedings (IEEE Piscataway, N.J. 2006) pp. 321-326.

21. Shanli Wang, Jian Li, Jie Chen, R. W. Collins, and A. D. Compaan, "Spectroscopic Ellipsometry and Atomic Force Microscopy Studies of rf Sputtered $Cd_{1-x}Mn_xTe$ Films", *31st IEEE Photovoltaic Specialists Conference, Orlando FL*, January 3-7, 2005 (IEEE, Piscataway NJ, 2005) pp. 480-483.

22. N.J. Podraza, Chi Chen, D. Sainju, O. Ezekoye, M. W. Horn, C. R. Wronski, and R. W. Collins, "Transparent Conducting Oxide Sculptured Thin Films for Photovoltaic Applications", *Mater. Res. Soc. Symp. Proc.* **865,** 273-278 (2005).

23. J. Chen, J. Li, D. Sainju, K.D. Wells, N.J. Podraza, and R.W. Collins, "Multilayer Analysis of the CdTe Solar Cell Structure by Spectroscopic Ellipsometry", *Proc. 4th World Conference on Photovoltaic Energy Conversion*, (IEEE, Piscataway NJ, 2006), p. 475.

24. Robert W. Collins, Alvin D. Compaan, Sylvain Marsillac, Anuja Parikh, Jie Chen, and

Jian Li, "Optical Analysis of II-VI Alloys and Structures for Tandem PV" *FY07 DOE Review* (April 17-19, 2007).

25. Jian Li, Jason A. Stoke, Nikolas J. Podraza, Deepak Sainju, Anuja Parikh, Xinmin Cao, Himal Khatri, Nicolas Barreau, Sylvain Marsillac, Xunming Deng, and Robert W. Collins, "Analysis and optimization of thin film photovoltaic materials and device fabrication by real time spectroscopic ellipsometry" *Proceedings of Society of Photo-Optical Instrumentation Engineers* (in press, August 29, 2007).

8.2   Poster or oral presentations published on CDROM or Web site

1. "Preparation and characterization of monolithic HgCdTe/CdTe tandem cells," S. L. Wang, J. Drayton, V. Parikh, A. Vasko, A. Gupta, and A.D. Compaan, Presented in MRS Fall Meeting, Boston, 29 Nov. – 4 Dec., 2004, L7.5.

2. "Optical studies on chloride-treated RF sputtered CdMnTe films," S. L.Wang, S. H. Lee, A. Gupta, and A.D.Compaan, Presented in MRS Fall Meeting, Boston, 29 Nov. – 4 Dec., 2004, L5.39.

3. "CdTe: How Thin Can It Be and How Does Chloride Activation Change grain Boundaries," Alvin D. Compaan, Akhlesh Gupta and X. Liu, Presented in Solar Energy Technology Program Review Meeting, Denver, CO, Oct. 25-28, 2004.

4. A.D. Compaan, R.W. Collins, D.M. Giolando, X. Mathew, S.L. Wang, V. Parikh, J. Chen, and J. Li, DOE Solar Energy Technologies Program FY2005 Annual Report (Proceedings, Program Review Meeting, Nov. 7-10, 2005, Denver, CO).

5. A.D. Compaan, R.W. Collins, V. Parikh, X. Mathew, D. Giolando, S.X. Marsillac, Anuja Parikh, Jie Chen, & Jian Li, "Sputtered II-VI Alloys and Structures for Tandem PV," DOE Solar Energy Technologies Program Review/Peer Review Meeting, Denver, Apr 17-19, 2007. Manuscript available at: http://www1.eere.energy.gov/solar/review_meeting/pdfs/p_17_compaan_univ_toledo.pdf

9. Project personnel

9.1 Research assistant professors

Akhlesh Gupta (Ph.D. Indian Institute of Technology, Delhi)(50% time, 12/9/03—7/05)

Diana Shvydka (Ph.D., U. of Toledo, 5/2002) (50% time 12/9/03—10/30/06)

9.2 Visiting Research Scholars

Xavier Mathew, on sabbatical from: Energy Research Center (CIE), UNAM, Apdo. P. 34, Temixco, Morelos, 62580, Mexico. (100% time 08/01/05- 07/31/06)

9.3 Postdoctoral Associate
Shanli Wang   (Ph.D. Shanghai Inst. Of Technical Physics, 1997)(50% time, 12/09/03—6/05)

Jennifer Drayton, (1/1/06-12/31/06)

Snigdha Gupta (Ph.D.) (100% time 2/07—7/30/07)

9.4   Graduate Students (Principal Advisor)
(Some students received support from other sources but made significant contributions to this work)

Viral Parikh (Compaan)
    M.S. and Ph.D. in progress

Jennifer Drayton (Compaan)
    Ph.D. December 2005, "Studies of RF Sputtered ZnTe:N and CdS for Photovoltaic Applications"

Jie Chen (Collins)
    M.S. in progress

Jian Li (Collins)
    M.S. and Ph.D. in progress

Todd Osborn (Giolando)
     M.S. 2005

9.5   Undergraduate students (advisor)
- Levi Gorrell, Univ. of Toledo, Summer REU student 2004 (Karpov)
- Molly Sauder, University of Toledo, senior project 05-06 "Spectroscopic Analysis of RF Sputtered CdMgTe Plasma" (Compaan)

- Sheriff Ceesay, Wilberforce University, summer REU student 2005 "Looking for Trace Elements by Optical Spectroscopy during CdS/CdTe Deposition" (Compaan)
- Mary Lin, Northwestern Univ., Summer REU student 2006, "Plasma Spectroscopy of RF Sputtering for CdS" (Compaan)
- Jason D. Owens, Univ. of Toledo, Summer REU student 2006, "Data Management in the CdTe Development Process" (Compaan)
- Craig McClellan, California University of Pennsylvania, summer REU student 2007, "Accelerated Degradation of CdTe Solar Cells with Differing Semiconductor Film Thicknesses" (Compaan)
- Ryan Zeller, Univ. of Toledo, Summer REU student 2007, "Optical Thickness Monitoring System for High Vacuum Deposition" (Compaan)

9.6 Laboratory Technical Assistants
(provided occasional assistance but were not funded on this project)

Terry Kahle
Robert Burmeister
Troy Berchem

REPORT DOCUMENTATION PAGE

Form Approved
OMB No. 0704-0188

1. REPORT DATE *(DD-MM-YYYY)* September 2008	2. REPORT TYPE Subcontract Report	3. DATES COVERED *(From - To)* 9 December 2003 – 30 July 2007

4. TITLE AND SUBTITLE
Sputtered II-VI Alloys and Structures for Tandem PV:
Final Subcontract Report, 9 December 2003 – 30 July 2007

5a. CONTRACT NUMBER
DE-AC36-99-GO10337

5b. GRANT NUMBER

5c. PROGRAM ELEMENT NUMBER

6. AUTHOR(S)
A.D. Compaan, R. Collins, V.G. Karpov, and D. Giolando

5d. PROJECT NUMBER
NREL/SR-520-43954

5e. TASK NUMBER
PVA72401

5f. WORK UNIT NUMBER

7. PERFORMING ORGANIZATION NAME(S) AND ADDRESS(ES)
Dept. of Physics and Astronomy
The University of Toledo
Toledo, Ohio 43606

8. PERFORMING ORGANIZATION REPORT NUMBER
XAT-4-33624-06

9. SPONSORING/MONITORING AGENCY NAME(S) AND ADDRESS(ES)
National Renewable Energy Laboratory
1617 Cole Blvd.
Golden, CO 80401-3393

10. SPONSOR/MONITOR'S ACRONYM(S)
NREL

11. SPONSORING/MONITORING AGENCY REPORT NUMBER
NREL/SR-520-43954

12. DISTRIBUTION AVAILABILITY STATEMENT
National Technical Information Service
U.S. Department of Commerce
5285 Port Royal Road
Springfield, VA 22161

13. SUPPLEMENTARY NOTES
NREL Technical Monitor: Fannie Eddy

14. ABSTRACT *(Maximum 200 Words)*
The major objectives of this subcontract were to explore, prepare, and test the candidate II-VI materials for top cells in two-junction devices with either monolithic two-terminal or mechanically stacked four-terminal structures. We developed two candidate alloys, CdMnTe, and CdMgTe by RF sputtering. The critical chloride treatments and related material studies revealed that CdMgTe is superior to CdMnTe. In the second year of this project, much of the effort was to develop the CdMgTe alloy. The goal of these efforts was to optimize the film deposition conditions and chloride treatments, and to identify the efficiency-limiting factors in a single-junction CdTe/CdS device that can lead to the goal of 25%-efficient tandem structures fabricated using polycrystalline thin films. The present report is the final report covering all three Phases.

15. SUBJECT TERMS
PV; sputtering alloys; tandem structure; polycrystalline; thin films; deposition; structural property; quantum efficiency; device; II-VI alloys.

16. SECURITY CLASSIFICATION OF:

a. REPORT Unclassified	b. ABSTRACT Unclassified	c. THIS PAGE Unclassified	17. LIMITATION OF ABSTRACT UL	18. NUMBER OF PAGES	19a. NAME OF RESPONSIBLE PERSON 19b. TELEPHONE NUMBER *(Include area code)*

Standard Form 298 (Rev. 8/98)
Prescribed by ANSI Std. Z39.18

F1146-E(09/2007)